CHALMERS
UNIVERSITY OF TECHNOLOGY

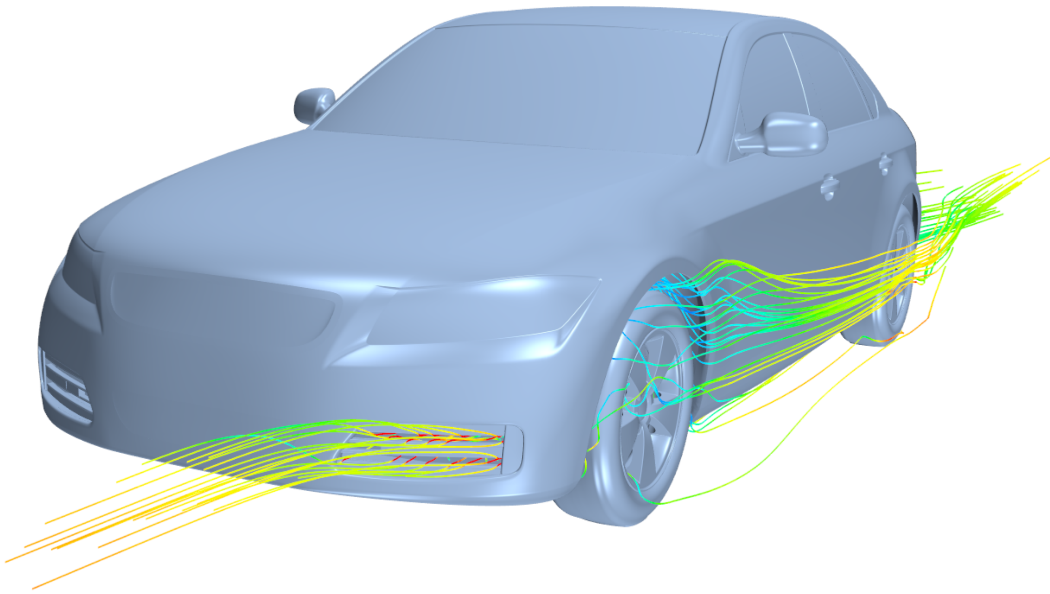

CFD Study of Optimal Under-hood Flow for Thermal Management of Electric Vehicles

Master's thesis in Applied Mechanics

JOHAN NORDIN

Department of Applied Mechanics
CHALMERS UNIVERSITY OF TECHNOLOGY
Göteborg, Sweden 2017

Master's thesis 2017:40

CFD Study of Optimal Under-hood Flow for Thermal Management of Electric Vehicles

JOHAN NORDIN

Department of Applied Mechanics
Division of Vehicle Engineering and Autonomous Systems
Chalmers University of Technology
Göteborg, Sweden 2017

CFD Study of Optimal Under-hood Flow for Thermal Management of Electric Vehicles
JOHAN NORDIN

Master's Thesis 2017:40
ISSN 1652-8557
Department of Applied Mechanics
Division of Vehicle Engineering and Autonomous Systems
Chalmers University of Technology
SE-412 96 Göteborg
Sweden
Telephone: +46 (0)31 772 1000

Cover: Streamlines colored by velocity through the heat exchanger of configuration B.8.

Chalmers Reproservice
Göteborg, Sweden 2017

CFD Study of Optimal Under-hood Flow for Thermal Management of Electric Vehicles
Master's thesis in Applied Mechanics
JOHAN NORDIN
Department of Applied Mechanics
Division of Vehicle Engineering and Autonomous Systems
Chalmers University of Technology

Abstract

To improve fuel economy of conventional vehicles and the driving range of electric vehicles, reducing the aerodynamic drag is of particular interest. As electric vehicles typically have lower cooling power requirement, reducing the aerodynamic drag induced by cooling air is of utter importance.

This study investigates alternative under-hood cooling flow solutions, with the target of reducing cooling drag for battery electric vehicles (BEV). Two different approaches of positioning the vehicle's heat exchangers (in series and in parallel) with a number of different air inlet and outlet configurations have been evaluated using CFD simulations. The geometry of the open grille DrivAer Model have been used to a large extent in this work, including a simplified electric powertrain and an alternative cooling module. For this work, a Reynolds-Averaged Navier-Stokes (RANS) method utilizing the k-ε turbulence model have been implemented in the commercial CFD software STAR-CCM+.

The results show that a similarly low cooling drag can be obtained from positioning heat exchangers both in series and in parallel. When heat exchangers are positioned in parallel, the results indicate high mass flow rate and low drag potential for side positioned inlets including air outlets located at the front arc of the wheel houses. Furthermore, results indicate that low positioned air inlets are more drag efficient than those positioned higher on the front bumper. The results of this study should serve as an suggestion towards under-hood cooling flow solutions for battery electric vehicles.

Keywords: CFD, DrivAer Model, Notchback, Thermal management, Electric vehicles, Cooling drag, Under-hood.

Preface

This report is a result of a master thesis project carried out during the spring of 2017 at ÅF Industry AB in Göteborg. The objective of the project was to investigate under-hood cooling flow solutions for BEV:s. The project has been a cooperation with NEVS AB.

Acknowledgements

First of all, I would like to thank everyone that have contributed to this project. A special thanks to Dr. Jan Östh, Group Manager at ÅF Industry for the opportunity to work on this project and for his support and guidance throughout the project.

Great thanks to everyone at Technical Analysis which made my time at ÅF Industry very enjoyable.

Also, great thanks to Dr. Mohammad El-Alti, Lead Engineer CFD & Thermal CAE at NEVS for this project opportunity and to my examiner, Professor Simone Sebben at Chalmers.

Furthermore, I would like to thank Daniel Egenvall, Engineer at NEVS, for contributing with CAD-geometry used in this work.

Lastly, thanks to CD-Adapco for providing license for their CFD software STAR-CCM+ and to BETA CAE Systems for providing license for ANSA.

Johan Nordin, Göteborg, May 2017

Contents

Nomenclature

Abbreviations	
BEV	Battery Electric Vehicle
CFD	Computational Fluid Dynamics
EM	Electric Motor
ESS	Energy Storage System
EV	Electric Vehicle
ICEV	Internal Combustion Engine Vehicle
LES	Large Eddy Simulation
NEVS	National Electric Vehicle Sweden
OEM	Original Equipment Manufacturer
PC	Power Converter
PHEV	Plug-in Hybrid Electric Vehicle
PID	Property ID
pp	Percentage point
RANS	Reynolds-Averaged Navier-Stokes
TMS	Thermal Management System
TUM	Technical University of Munich
Symbols	
δ_{ij}	Kronecker delta
ν	Kinematic viscosity
ν_t	Turbulent viscosity
$\overline{v}_i$	Time-averaged velocity, i:th component
ρ	Density
ε	Turbulent dissipation rate
C_d	Drag coefficient
C_P	Pressure coefficient
F_d	Drag force
k	Turbulent kinetic energy
p	Pressure
P_i	Inertial porous resistance tensor
P_v	Viscous porous resistance tensor
v_i'	Fluctuating velocity, i:th component
v_i	Instantaneous velocity, i:th component
x_i	Spatial, i:th component
y^+	Dimensionless wall distance

List of Figures

1
Introduction

1.1 Background

The interest in Electric vehicles (EV) have increased due to growing concern regarding the CO_2-emissions associated with Internal Combustion Engine Vehicles (ICEV). Annually published academic reports on electric vehicles have increased by at least five times since 2004 [1] and new registrations of Battery Electric Vehicles (BEV) have increased more than 70% annually for three consecutive years (2012-2015). China alone accounted for 45% of all new registered BEV:s in 2015 and is together with United States the two largest players in the market [2]. However, Japan and many countries in Europe such as Germany, France and Norway have shown an increasing interest in BEV:s. The combined sales of BEV:s and Plug-in Hybrid Electric Vehicles (PHEV) reached 1.26 million by 2015 which is 100 times more than in 2010 [2]. Furthermore, the industry-wide cost of Lithium-ion battery packs have declined from above 1000 USD to around 450 USD per kWh between 2007-2014, according to [3]. While the energy density of Lithium-ion batteries increased from 200 to above 500 Wh/liter between 1991-2005 [4].

Even with great progress in battery development, the driving range of BEV:s is still far behind that of conventional ICEV:s. The capacity of the battery pack is very limited as the total energy content in the battery of an BEV is one magnitude lower than the fuel energy in an ICEV [5]. In order to increase the driving range it is generally favourable to decrease the aerodynamic drag and thus the fuel/energy consumption. This is of particular interest for BEV as aerodynamic drag account for a substantial amount of the total energy losses due to a generally efficient electric powertrain.

The lowest aerodynamic drag is typically obtained with closed frontal grilles and no cooling air through the engine compartment. This scenario is generally not feasible as the powertrain can overheat and possibly cause sustained damage. Instead manufactures use active grill shutters to reduce the air-flow when the need for under-hood cooling is reduced. As the powertrain of BEV:s is considerably more efficient than that of a conventional combustion engine vehicle [6], less waste energy is available to ensure climate comfort. Hence, it is of utter importance to reduce the aerodynamic drag caused by cooling air and to ensure an efficient thermal management, as these factors directly influence the driving range of BEV:s. During the early design of an BEV, there exists large possibilities to explore and use alternative design solutions than those that are traditionally used. In later stages of the design and construction phases ad-hoc modifications are often limited and typically very expensive.

1.2 Purpose

The purpose of this thesis is to investigate under-hood cooling flow solutions for BEV:s. The thesis can be divided into two parts, one literature review part and one simulation part of cooling flow solutions. Based on the literature review, concepts of possible improvements will be evaluated using Computational Fluid Dynamics (CFD).

1.3 Limitations

The project is limited in time to 20 weeks. Computational resources are limited by those available at ÅF. The exterior geometry is limited to the notchback DrivAer Model with smooth underbody. The existing under-hood components of the model are replaced by a simplified electric powertrain, not representing a complete under-hood compartment of an BEV. Furthermore, the computations are solved for steady-state solution discarding heat transfer coupling.

2

Thermal Management of BEV:s

In this chapter, an introduction to thermal management of BEV:s is presented. Firstly, the propulsion system and the thermal management system of an BEV are explained. Secondly, a literature review of automotive under-hood flow management is presented.

2.1 Propulsion system

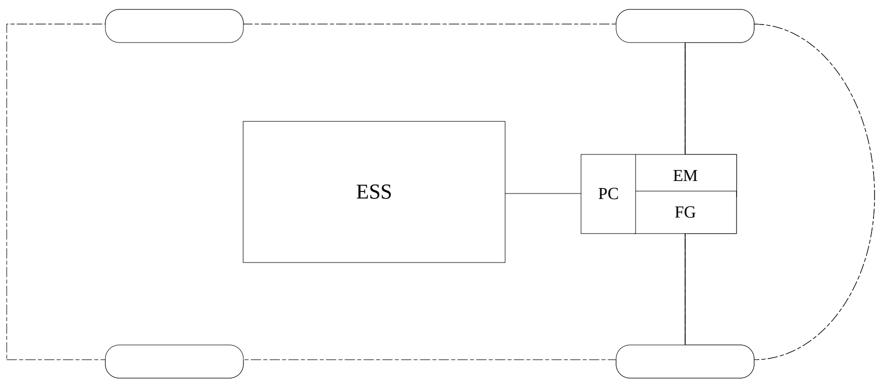

Figure 2.1: *Schematic figure of a simplified electric propulsion system. ESS = Energy Storage System, PC = Power Converter, EM = Electric Motor, FG = Fixed Gearing.*

The propulsion system of an BEV is relatively flexible as the energy flow is mainly through electrical wires rather than mechanical links [7]. Thus, the size of the propulsion system is generally smaller than that of a fuel driven vehicle, which enable greater packaging flexibility in the under-hood compartment. The Energy Storage System (ESS) is typically located in the middle of the car, underneath the seats. The ESS is connected to a Power Converter (PC) that can regulate the power from the ESS to the EM. For front-wheel driven electric cars, the power converter and EM is usually located in the under-hood compartment. Generally, a single-speed gearbox is then connected between the EM and the drive shafts.

2.1.1 Electric motor

The Permanent Magnet Synchronous Motor is the dominating type of EM:s [1]. Among others, it can be found in the popular electric vehicles, Kia Soul EV, Nissan

Leaf and Hyundai IONIQ [8][9][10]. Keeping the temperature in the motor within the operating temperature range is crucial to avoid decreasing intrinsic coercivity of the permanent magnets at high temperatures. This will cause demagnetization of the magnetic material [11]. Most Original Equipment Manufactures (OEM) are using liquid based cooling for the motor [1]. The excessive heat from the motor and the gearbox is often dissipated in the radiator or should preferably be used for heating purposes of the cabin or ESS if desired.

2.1.2 Power converter

The Power Converter (PC) is usually connected between two devices where a conversion of electric energy is necessary. In EV:s, the PC is connected between the ESS and EM to regulate power output and to convert direct current (DC) to alternating current (AC). Power converters are classified by the type of input and output electrical energy and can often be refereed as *Power inverter* in EV:s.

2.1.3 Energy storage system

The ESS is the energy source of an BEV, corresponding to that of the fuel in a conventional vehicle. The ESS is often positioned in the middle of the vehicle below the passenger seats. The Lithium-ion type is most common battery chemistry which roughly has an operating temperature range of 0 to 45 degrees. Liquid-based cooling of the ESS is most commonly used method among BEV:s [1].

2.2 Thermal management system

The purpose of the Thermal Management System (TMS) of an BEV is to keep temperatures of the propulsion system within its operating temperature range to ensure functionality and safety. At the same time provide cabin comfort for all passengers. These requirements have to be fulfilled at all driving and weather conditions.

Dependent on driving situation, the thermal requirement from the components of the propulsion system can alter. In hot ambient temperature conditions, usually all components of the propulsion system, including the cabin, demand a cooling need. In cold ambient temperature conditions, the majority of the subsystems requires heating, except possibly the EM. The TMS must therefore be able to satisfy both cooling and heating requirements for the propulsion system and the cabin.

Several of the components from a cooling system of an combustion vehicle is included in the TMS of an BEV, e.g., radiator, condenser, axial fans etc. A schematic figure of an simplified electric thermal management system can be seen in Fig. [2.2]

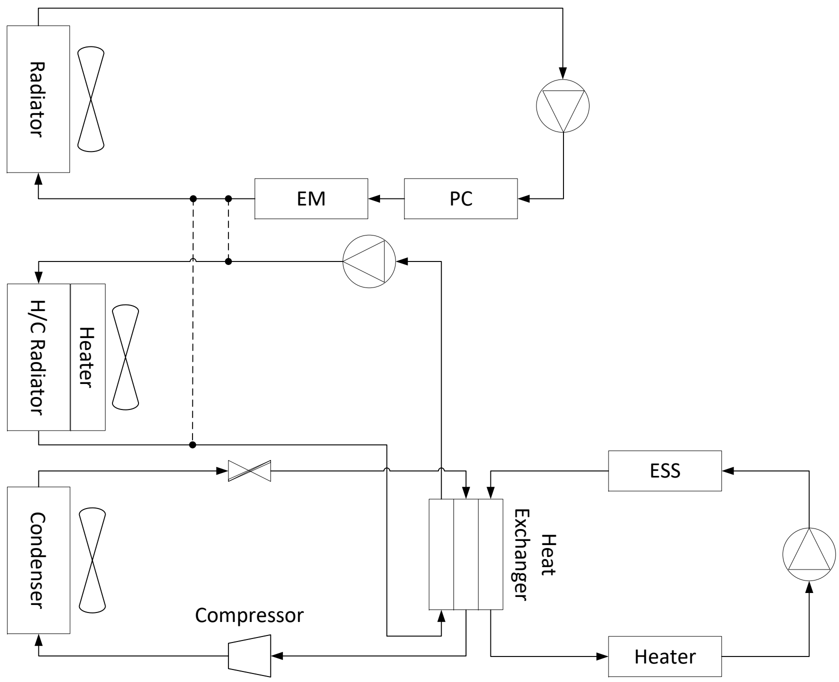

Figure 2.2: *Schematic figure of a simplified thermal management system. Redrawn from [12].*

2.2.1 Radiator

It is designed to maximize heat transfer capability by increasing the surface area which is in contact with ambient air. The radiator is used to dissipate excessive heat from the propulsion system, specifically the EM and PC which can be seen in Fig. [2.2]. Hot coolant from the EM, flow through the radiator where heat is transferred from the coolant to the core of the radiator. As air of ambient temperature flow through the core, heat is dissipated to ambient air. The system is most effective when there is a large temperature difference between ambient air and the coolant but also when the surface area of the core is maximized. To further increase the heat transfer rate, an axial fan can be mounted behind the radiator for increased mass flow rate. In BEV:s the operating temperature of the propulsion system is significantly lower than that of a conventional fuel driven system, which reduce heat dissipation in warmer ambient conditions.

2.2.2 Heat pump

The heat pump moves energy or heat by consuming electricity. Heat can be transferred from cold to warm areas and vice verse. The heat pump has an advantage in efficiency compared with other alternatives, such as electric heaters. The heat pump mainly consist of four components, evaporator, condenser, compressor and an expansion valve including a refrigerant which is carrying the energy through the cycle. The refrigerant is first evaporated in the evaporator through absorption of heat. The vapor is then compressed in the compressor, increasing pressure and the temperature such that more energy can be transferred out from the condenser whereas the refrigerant condenses. The refrigerant then expands in the expansion valve before completing the cycle at the evaporator. In Fig. [2.2], the evaporation occurs in a heat exchanger connected with the ESS coolant loop and the cabin comfort loop. Excessive heat from the ESS is transferred by a coolant to the heat exchanger where the evaporation occurs. The condenser is often positioned in the front of the vehicle, susceptible to ambient air. Such that heat is dissipated for the condensation of the refrigerant. An axial fan can be mounted behind the condenser to improve the heat transfer at stand still conditions.

Among the five most sold electric vehicles in the United States, Europe and Japan during 2014-2015 [1], at least three cars are equipped with a heat pump, them being Nissan Leaf [13], Renault Zoe [14] and BMW i3 [15].

2.2.3 Electric heater

The electric heater convert electric current to heat by a resistor. Functionality in all types of climates is an advantage of electric heater, as the heat pump become less efficient for extreme cold and warm outdoor temperatures. The electric heater is often used to provide additional heat to the ESS and/or the cabin.

2.2.4 Heating and air conditioning

A separate heat exchanger and fan is used to provide cold or warm air into the cabin. Energy is generated by an electric heater to increase the temperature of the liquid inside the heat exchanger. Alternatively or in addition to the electric heater, warm coolant from the cooling loop of the propulsion system can be used.

In Fig. [2.2] the heating and air conditioning loop is connected to the heat pump circuit through a heat exchanger. Energy of the coolant from the heating and air conditioning loop is utilized for the evaporation process, colder coolant is then pumped through the cabin heat exchanger. Thus, cold air can be provided to the cabin from the fan.

2.3 Under-hood flow management

The air-flow entering from the front grille (air inlet) is influenced by many components obstructing its way. Even small geometry details can affect the flow direction and impact the under-hood cooling performance. Especially, the cooling package including fan, fan shroud and heat exchangers have considerable impact [16].

The cooling package of an ICEV is often positioned at the front-end, in close proximity to the grilles. The condenser, radiator and fan shroud are often aligned one after another in the direction of the air-flow. This was proposed by Simonin et al. [17] to reduce frontal area and volume of the cooling module. However, the packaging of the electric powertrain is less restricted than that of ICEV:s, using electrical wires and cables rather than mechanical links. Thus, greater design space can possibly be provided for designing the cooling package for BEV:s.

For an air-to-liquid heat exchanger, characteristics such as temperature distribution of the liquid, temperature distribution of air downstream of the core as well as the velocity profile over the heat exchanger core are of great importance to the performance. The air-flow velocity profile over the heat exchanger core is influenced by many factors, including position and size of inlets and outlets, respectively. As the heat exchangers are traditionally positioned at the front end, high mass flow rate is provided by the ram-air. Outlets are mainly located at the wheel houses and at the exhaust tunnel to enable air to exit from the engine compartment. Typically, the heat exchangers and air inlets of BEV:s is also located at the front-end of the vehicle whereas the outlets are located at the wheel houses or at the floor of the engine compartment. In addition to the influence of outlets on cooling performance, the CFD study [18] suggest that they also influences the overall drag of the vehicle by redirecting the air-flow exiting the engine compartment.

2.3.1 Methods of cooling drag reduction

Aerodynamic drag is the second largest contributor to reduction of electric range behind vehicle mass [19]. The cooling drag is often defined as the drag of the vehicle with frontal openings compared to that of the vehicle without openings. Generally for conventional vehicles, the cooling drag is approximately 10% of the global aerodynamic drag. One study suggests that it's up to 25% [21]. Efficient air management is crucial for electric vehicles as the propulsion system is prone to overheating and the small amount of waste heat should ideally be used for cabin comfort. The overall cooling power in EV:s are significantly lower than that of its counterpart. An conceptual idea is therefore to reduce the mass flow rate of cooling air through the heat exchangers and the engine compartment as the cooling air is generally contributing to the drag of the vehicle. In the development of the PHEV Chevrolet Volt, the engineers managed to reduce the overall drag coefficient by 0.010, by closing much of the upper grille [19].

Results from the study by Zhang et.al [20], show that the cooling drag can be reduced by reducing the opening area of the front grille and therefore also reducing the total vehicle drag. The conclusion coincide with that from a experimental study [21]

By closing front-end inlets, drag reductions up to 0.020 were demonstrated in a wind tunnel study of the electric Tesla Model S [22]. The same wind tunnel study also indicates a higher aerodynamic drag reduction by closing the inlets positioned further up than that of those further down, which coincide with the result from [23] which conclude that closing the upper grille is more efficient than closing the lower grille, if a reduction in cooling air is desired.

3
Geometry and Configurations

In this chapter, an introduction to the original geometry of the DrivAer model is given. Furthermore, the modified and additional geometries that are used for Concept A and Concept B are presented.

3.1 DrivAer Model

A lot of research in automotive aerodynamics have been done on simplified generic bodies such as the Ahmed model. Observed flow phenomena from the Ahmed model has substantially increased the general knowledge of basic flow structures around bluff bodies. However, by using such models, automotive aerodynamic research is restricted by the simplified geometry. Hence, detailed flow around mirrors, underbody and under-hood flow cannot be produced. At the same time, aerodynamic development on production vehicles are limited by the confidentiality and a very limited time span due to design changes.

The DrivAer Model is a generic passenger car model for aerodynamic investigations developed by Technical University of Munich (TUM) together with Audi AG and BMW Group [24]. The geometry of the DrivAer Model is free to download and available on the website of TUM [25]. The purpose was to develop a realistic aerodynamic car model which allow for detailed flow investigations to close the gap between widely used simplified generic models and specific car models with short time span. The DrivAer Model is based on CAD geometry from the passenger cars, Audi A4 and BMW 3 series [24], that allow for high versatility of aerodynamic investigations. The DrivAer Model comes with three different rear-top geometries as well as three different underbody geometries. Mirrors and wheels are interchangeable which allow for further external aerodynamic investigations.

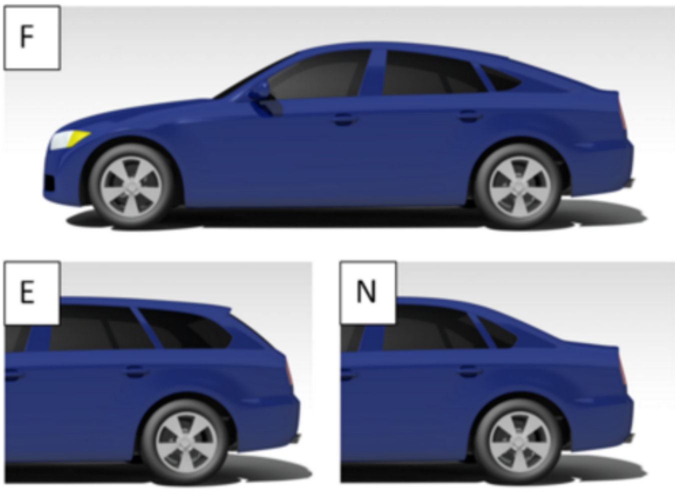

Figure 3.1: *Rear-top geometries of the DrivAer Model, F - Fastback, N - Notchback, E - Estateback. Image taken from [25].*

In the introduction paper [24] about the DrivAer Model, pressure measurement data was obtained in the wind-tunnel at TUM using a scaled 1:2.5 DrivAer Model. The data indicate that the DrivAer Model is aerodynamically non-optimized as the drag coefficient compared to that of the original Audi and BMW is slightly higher, yet it is in the range of other mid-size passenger cars [24].

Since the introduction, the DrivAer Model has been subject to a number of aerodynamic studies. One study by Shine et at. [26], investigated the external flow and drag coefficients of the three rear-top geometries using steady-state simulations in OpenFOAM. Drag coefficients were predicted within 0.5% to 12% compared to the results published by Heft et al. [24].

Another study of the DrivAer Model was also performed by Ashton et al. [27] evaluating RANS and Detached eddy simulation methods. They found that a variety of RANS methods were consistently underpredicting drag coefficients of the estate and fastback models by up to 41 counts.

However due to recent interest in cooling drag investigations, an open grille version of DrivAer Model was introduced by Wittmeier and Kuthada [23]. The geometry included a simplified engine compartment and a cooling module, which can be seen in Fig [3.2].

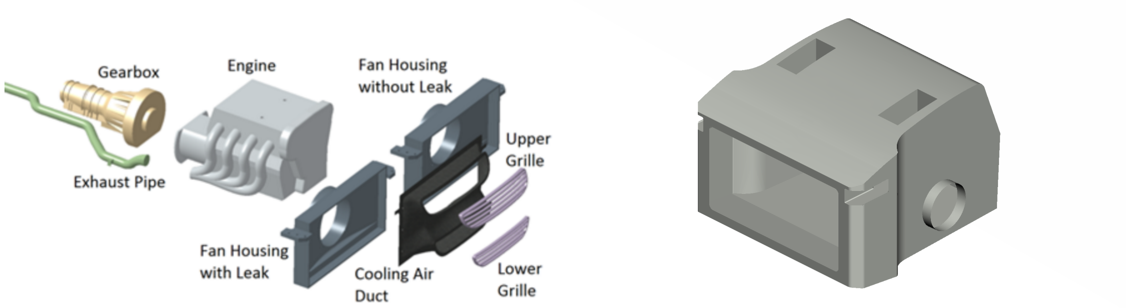

Figure 3.2: *Original engine bay configuration of the DrivAer Model (left), image taken from [25]. Original engine compartment geometry of the DrivAer Model (right).*

The under-hood compartment was designed such that no changes of the exterior of the car was necessary, in order to keep all previous work relevant for future comparison. At the front-end of the car, there are two grilles which act as air inlets. The cooling air can then flow into the engine compartment and out through the front drive shaft holes or exhaust tunnel exit. The space available for the cooling package allow for modified designs of grill shutters, air ducts and fan housing. The original fan housing comes in two configurations, with and without leakage flow. Within the fan housing a pressure drop region for modelling of heat exchanger is available.

3.2 Configurations

In this section the original geometry and the modified geometry of Concept A and Concept B, that have been investigated in this thesis, are presented and explained.

In this work the notchback and the smooth underbody geometries from the DrivAer Model will be used entirely for all the simulation work. As the geometry is supposed to represent an electric vehicle, the combustion engine, exhaust pipe and gear box from the open grille DrivAer Model are replaced by a simplified powertrain of an EV. This geometry is provided by NEVS and can be seen in Fig. [3.3]. The heat exchangers are modeled as porous media using pressure drop regions derived from the original geometry of the DrivAer Model.

3.2.1 Concept A

For Concept A, the original pressure drop region is split into one region for the radiator and one for the condenser, see Fig. [3.4]. The frontal area of the pressure drop regions is kept while the depth of the region is divided, resulting in two 25 mm pressure drop regions. The space between these regions are set to 23.5 mm such that the regions are kept within the original fan housing geometry. The enclosure for pressure drop regions is based on the original fan housing geometry, seen in Fig. [3.2]. The purpose of the enclosure (seen in Fig. [3.5]) is to ensure no leakage flow around the cooling package, thus mass flow rate through the grilles is equal to that

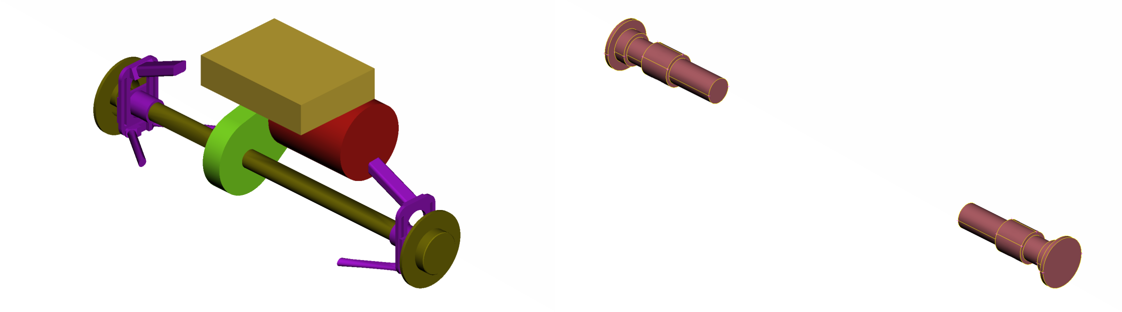

Figure 3.3: *Left: Powertrain geometry consisting of electric motor (red), power converter (yellow), gearbox (green), drive shafts (olive green) and suspension (purple). Right: Rear drive shafts (red).*

Figure 3.4: *The original pressure drop region (heat exchangers modeled as porous media) from the DrivAer Model (left) and the pressure drop regions used for Concept A (right).*

through the pressure drop regions. The enclosure used in concept A is also designed to provide no blockage behind the pressure drop regions in order be able to make easier comparison between different concepts. Modeling of the fan behind the heat exchanger is also discarded for this reason. The complete cooling package used in Concept A can be seen in Fig. [3.5].

Figure 3.5: *Left: Cooling module used in Concept A. Right: Cross section of cooling module used in Concept A.*

In addition to the outlet at the drive shaft holes of the engine compartment, an additional outlet through the floor of the engine compartment is designed. This additional outlet is not included in the standard geometry for Concept A, but as a configuration . The outlet is created to investigate the effects of air exiting from the middle of the floor, replacing the exhaust tunnel outlet. The width is 696 mm and the depth measured normal to the inclined surface is 37 mm. The inclined surface create an angle of 22 degrees to the horizontal plane. The outlet is placed in a low pressure region between the two front wheels.

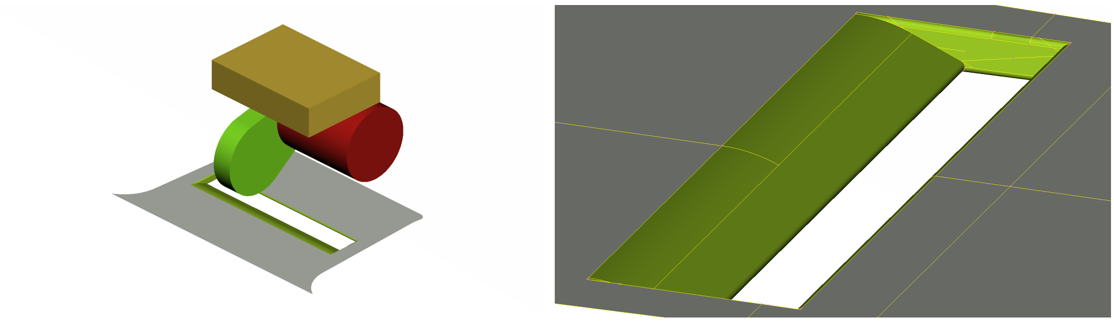

Figure 3.6: *Additional outlet through the floor together with the electric powertrain (left), zoom-in of the same outlet (right).*

3.2.2 Concept B

This concept utilizes parallel positioned heat exchangers in contrast to the previous concept where they are serially situated. As a result of the literature presented in Section [2.3.1], the upper inlet is now closed leaving the lower inlet open, with the target of reducing drag. This specific inlet configuration is also common among many electric vehicles including, Nissan Leaf, Renault Zoe, BMW i3, Tesla Model S, Hyundai IONIQ etc. However, in addition to the lower inlet, two new inlets are opened on each side of the lower inlet to add design alternatives.

The complete cooling package used for Concept A is now modified to be suitable for Concept B. Firstly, the size of the heat exchangers from Concept A have to be reduced in order for them to be arranged in parallel and still fit inside the vehicle. The width is therefore reduced from 787 to 775 mm and the heat exchangers is set at an 4.4 degree angle from the lateral axis. Since the upper inlet is closed, the height of the old heat exchangers is reduced accordingly, resulting in a reduction from 400 mm to 166 mm. The combined frontal area of both the condenser and the radiator for Concept B now account for 81% of frontal heat exchanger area of Concept A.

A new air guide is required, as the upper inlet is closed and two new inlets open. The air guide connect the lower inlet and the new side inlets with the heat exchangers. Geometry and inspiration from the old air guide is used to design the new air guide which should allow for straight cooling flow towards the side of the heat exchangers. To the left in Fig. [3.7], the modified air guide and the grilles can be seen, while to the right in Fig. [3.7], the condenser and radiator can be seen. The engine compartment required an extension laterally to fit the cooling package. The new engine compartment used for Concept B can be seen to the left in Fig. [3.8]. In order for the flow to exit smoothly from the outer part of the heat exchangers, two

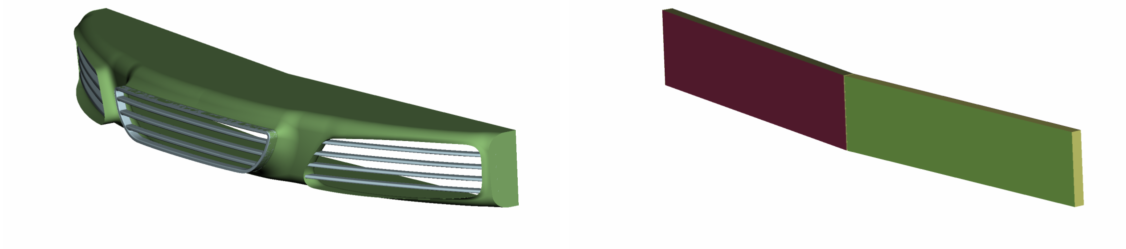

Figure 3.7: *Left: Air guide and grilles. Right: Condenser (green) and radiator (red) used in Concept B.*

outlets are created on the front face of the wheel houses. These additional outlets are (similarly to the outlet through the floor in Concept A) a design configuration in Concept B. As the outlets are located right behind the heat exchangers, they are believed to absorb most of the air entering from the side inlets. The height of the outlet is 260 mm and the width is 200 mm and can be seen to the right in Fig. [3.8].

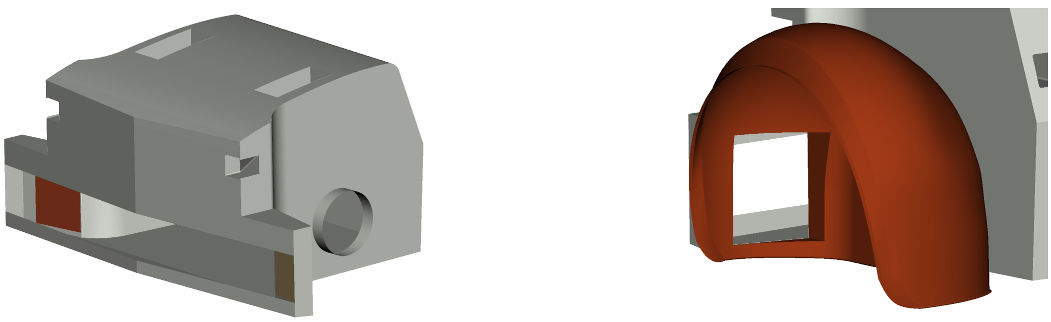

Figure 3.8: *Visualization of the engine compartment (left) and additional outlets through the wheel houses (right).*

4

Methodology

This chapter outlines the methods that are used in the thesis. Firstly, theory and modelling techniques that are used in this work are explained. Secondly, the geometry preparation that is performed in the software ANSA v17.1 is presented. Finally, the meshing and numerical settings are described which is entirely done in the software STAR-CCM+ v11.06.

4.1 Theory

4.1.1 Reynolds-Averaged Navier-Stokes

The computations carried out in this thesis solve the Reynolds-Averaged Navier-Stokes (RANS) equations. Steady RANS models are widely used in industries as it produces reasonably accurate results and is far more computational affordable than e.g., Large Eddy Simulation (LES) or Hybrid RANS-LES [27]. The RANS equations are derived from the governing equations of Navier-Stokes by decomposing the instantaneous velocity according to

$$v_i = \overline{v}_i + v_i', \tag{4.1}$$

where $\overline{v}_i$ is the mean value and v_i' is the fluctuating part. The decomposed Navier-Stokes equations are then time-averaged to become the RANS equations given as

$$\frac{\partial \overline{v}_i}{\partial x_i} = 0, \tag{4.2}$$

$$\frac{\partial \overline{v}_i \overline{v}_j}{\partial x_j} = -\frac{1}{\rho}\frac{\overline{p}}{\partial x_i} + \nu \frac{\partial^2 \overline{v}_i}{\partial x_j \partial x_j} - \frac{\partial \overline{v_i' v_j'}}{\partial x_j}, \tag{4.3}$$

where the last term on the right-hand side of Eq. [4.3] is called the Reynolds stress. This term is modeled using Boussinesq assumption given below

$$\overline{v_i' v_j'} = -\nu_t \left(\frac{\partial \overline{v}_i}{\partial x_j} + \frac{\overline{v}_j}{\partial x_i} \right) + \frac{2}{3}\delta_{ij} k, \tag{4.4}$$

where ν_t is the turbulent viscosity.

4.1.2 Turbulence modeling

In the commonly used eddy viscosity model, the k-ε turbulence model, the turbulent viscosity is modeled using two quantities, ε and k, according to

$$\nu_t = c_\mu \frac{k^2}{\varepsilon} \tag{4.5}$$

where k is the turbulent kinetic energy and ε is the turbulent dissipation rate. In the standard k-ε model c_μ is set to a constant value. The standard model tend to overpredict turbulent viscosity for flows with high mean shear rate or separated flows. For this reason Shih et al. [28] introduced a new k-ε eddy viscosity model with an appropriate turbulent viscosity formulation including a new modified ε-equation. This model is often called the Realizable k-ε turbulence model. In the new formulation of the model, c_μ is calculated from an expression instead of being a constant,

$$c_\mu = \frac{1}{A_0 + A_s U^{(*)} \frac{k}{\varepsilon}}, \tag{4.6}$$

where $U^{(*)}$, A_0 and A_s are dependent on the strain rate, rotation rate tensor and the angular velocity [28]. The modified ε-equation reads,

$$\frac{\partial \varepsilon}{\partial t} + \overline{v}_j \frac{\partial \varepsilon}{\partial x_j} = \frac{\partial}{\partial x_j}\left(\frac{\nu_t}{\sigma_\varepsilon}\frac{\partial \varepsilon}{\partial x_j}\right) + c_1 S\varepsilon - c_2 \frac{\varepsilon^2}{k + \sqrt{\nu\varepsilon}}, \tag{4.7}$$

where S is the mean strain rate and the coefficients c_1, c_2 and σ_ε are set to

$$\begin{cases} c_1 = 1.44, \\ c_2 = 1.9, \\ \sigma_\varepsilon = 1.2. \end{cases} \tag{4.8}$$

4.1.3 Wall treatment

Since exterior aerodynamics is associated with varying velocity scales it is difficult to construct a pure low y^+ or high y^+ mesh. For this reason, the boundary layer is modeled using a combination of low y^+ and high y^+ wall treatment, which is suitable for intermediate boundary layer resolutions. In regions where a fine mesh is obtained (y^+ ~1), the wall treatment resolves the viscous sublayer. Whereas for $y^+ > 30$, the viscous sublayer is not resolved, instead boundary conditions of wall shear stress, turbulent production, and turbulent dissipation are derived for the continuum equations. In the intermediate region a blending function is used to obtain the turbulent quantities [29].

4.1.4 Heat exchanger modeling

A common approach to modeling of heat exchangers is through a porous media. An additional source term is added to the momentum equations which includes the superficial velocity and porous resistance tensor [30]. For the porous region to be fully defined, appropriate resistance coefficients need to be specified. These can be determined by fitting a second order polynomial to the expression of pressure drop which reads,

$$\frac{\Delta p}{L} = -(P_i|v| + P_v)v \tag{4.9}$$

where P_i and P_v are the inertial and viscous porous resistance tensors, respectively and v is the superficial velocity through the medium. The best fit approximation of Eq. [4.9] is performed using the matlab function *polyfit*.

Data[1] of the pressure drop and the mass flow rate across both the condenser and the radiator are provided by NEVS. In order to find the superficial velocity, the average velocity is calculated using the mass flow rate and the frontal area of the real heat exchangers. The depth of the real heat exchangers does not correspond to the virtual ones, therefore the pressure drop values are scaled with the depth of the virtual heat exchangers to obtain the same total pressure drop across each heat exchanger.

To mimic the uni-directional flow through the heat exchangers the resistance coefficients for the lateral and vertical directions are increased by two orders of magnitude.

4.2 Numerical setup

4.2.1 Geometry preparation

The two main purposes of the work performed in ANSA is to clean the geometry of all intersecting surfaces, free edges and gaps in order to generate a CAD representation of the car that is suitable for meshing. And secondly, to divide the geometry in different Property ID:s (PID) which later translates into different surfaces when imported in STAR-CCM+. The advantages of the geometry being divided into different surfaces is that each surface can be assigned a specific boundary condition and mesh setting. E.g., the tire and the body of the car should be separated, since a rotating boundary condition is only desired on the tire and not on the body. This also allow for surface mesh refinement on specific parts of the car where it might be desired. Some examples are mirrors, a-pillars, c-pillars and the rear-end.

The original CAD geometry of the DrivAer Model can be seen in Fig. [4.1]. The first step is to divide the geometry in different PID:s. Since, one PID can not contain two different settings, it is therefore important to split the geometry where different settings is desired, i.e., mesh refinement. The work mostly consist of cutting existing surfaces using `Faces->Cut` and assigning a new ID to these surfaces using `Faces->Set PID`. In some locations the geometry consist of *Needle Faces* and *Collapsed Cons*. These issues are solved by releasing the CONS and Hot Points and re-create the surfaces using `CONS & Hot Points->Release` and then `Faces->New`.

[1]The data for the condenser and the radiator is not identical, resulting in non-symmetric heat exchangers in Concept B. The data is not presented in this report by request from NEVS.

Figure 4.1: *Original geometry of the exterior of DrivAer Model.*

Some parts from the original geometry also contain free edges (*Single Cons*), these are simply removed or connected with neighbouring faces. The final partitioning of the car including the under-hood parts, consists of 58 PID:s and can be seen in Fig. [4.2]. Before the model can be exported, the geometry need to be triangulated. The

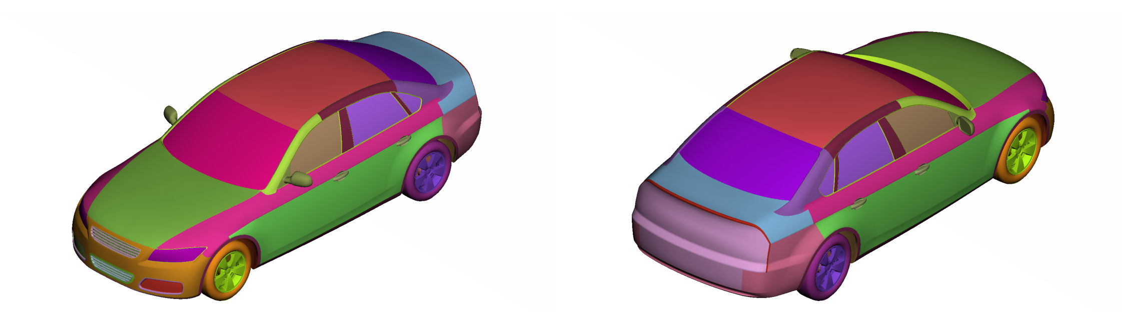

Figure 4.2: *Final PID geometry of the DrivAer Model.*

edges of each surface is first discretized using `Perimeter->Spacing->Auto STL`, it is important that the curvature is well represented which is achieved using an absolute *Chordal Deviation* of 0.02. The geometry is then triangulated and afterwards exported from ANSA as input-files (`.inp`).

The geometry is imported through the input-files to STAR-CCM+. Surfaces are then duplicated such that several parts can be created, each consisting of a set of surfaces enclosing a specific volume. The surface wrapper is then used to generate each of these volumes enclosed by a set of surfaces. It is important that these surfaces represent the true boundaries of the desired volume and that there exist no gap in-between. To capture the true geometry it is often necessary to use contact prevention tools. In case of reproducing geometry consisting of sharp and thin edges, contact prevention is necessary unless the triangulation size used for wrapping is very small(<10E-5). For the geometry of interest, contact prevention is used between floor and tires, grilles and its surrounding, the air guide and the heat exchangers, side-mirrors, spokes and tires. It is an iterative processes of finding wrapper settings together with suitable contact prevention to generate the desired geometry. Once the obtained surfaces are satisfactory the geometries are ready for surface re-meshing and volume meshing.

4.2.2 Meshing

The surface mesh size of the car is set to vary between 1 and 8 mm over the surface of the car. Small curvatures on the front-end of the car, is set to 2 mm and allowed to decrease down to 1 mm. In areas where large pressure gradients and medium level of curvature is expected, the size is set to 4 mm and minimum of 2 mm. Both surface refinement areas can be seen in Fig. [4.3]. The coarsest mesh of 8 mm is set to the hood, windshield, roof, side windows and doors which are considered regions where larger mesh size can be used. Between different surface mesh sizes the transition rate is set to *Medium* to avoid large discrepancy. The near-wall mesh is built to fit the All y^+ Wall Treatment in STAR-CCM+. 6 prism layers are used with a total height of 4 mm and a layer growth of 1.5. With these settings the non-dimensional y^+ values are mainly within the span of 1 and 40, see Appendix [A.1]. In order to

Figure 4.3: *Surface refinement areas, base size of 2 mm and minimum size of 1 mm (left), base size of 4 mm and minimum size of 2 mm (right).*

keep the volume mesh from growing too fast, the volumetric transition rate is set to *Very Slow* and refinement boxes around the vehicle are used to limit the volume cell size. Behind the rear-end and near the lower part of the car the size is prohibited by refinement boxes from growing larger than 8 mm in order to capture small changes in the flow field, this region can be seen in Fig. [4.4]. Further away from the

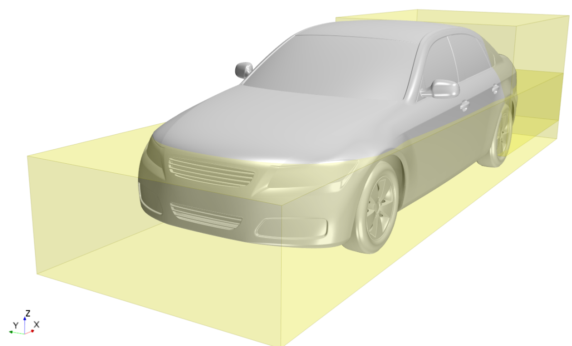

Figure 4.4: *Refinement box limiting the cell size at 8 mm (yellow).*

vehicle, refinement boxes are created for limiting the cell size to 16, 32 and 64 mm according to Fig. [4.5]. The mesh is then growing up to 256 mm towards the walls

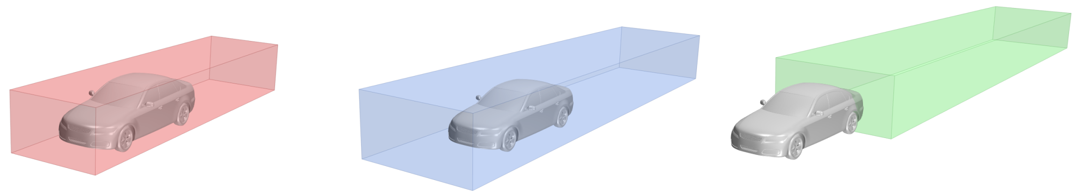

Figure 4.5: Refinement boxes limiting the cell size at 16 mm (red), 32 mm (blue) and 64 mm (green).

of the wind tunnel, except for the floor of the tunnel where the cell size is varying between 8 mm up to 128 mm.

For the engine compartment a constant size of 8 mm is used together with 3 prism layers. Within and neighbouring to heat exchanger regions, 4 mm cells are used. The final volume mesh consist of approximately 43 million cells (depending on geometry configuration) where reduction of approximately 5 million cells is obtained by disabling the surface meshing options, curvature and proximity refinement. In Fig. [4.6] a plane section of the final volume mesh at y=0m can be seen.

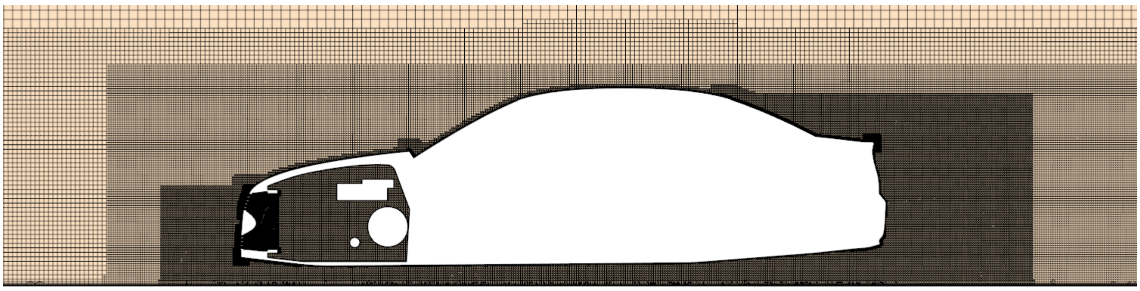

Figure 4.6: Volume mesh in a plane section located at y = 0m (centerline of the vehicle).

4.2.3 Physics models

The computations of this thesis are carried out in the commercial CFD software STAR-CCM+. A Steady RANS approach with the Realizable k-ε model turbulence model is implemented in the software. The simulations are computed without the energy equation, thus heat characteristics of the motor and the heat exchangers are discarded. A complete list of all physics models used can be seen in Table [4.1].

Physics Models
Cell Quality Remediation
Constant Density
Exact Wall Distance
Gas
Gradients
K-Epsilon Turbulence
Realizable K-Epsilon Two-layer
Reynolds-Averaged Navier-Stokes
Segregated Flow
Steady
Three Dimensional
Turbulent
Two-Layer All y+ Wall Treatment

Table 4.1: *Physics models used by the solver during computations.*

4.2.4 Boundary conditions

The computations are carried out in a virtual wind tunnel with dimensions 12 x 12 x 52 m at 120 kph. The center of the front wheel is positioned 15 m from the inlet of the wind tunnel, resulting in approximately 1/3 of the wind tunnel in front of the vehicle and 2/3 behind. The inlet and outlet of the wind tunnel are set to *Velocity Inlet* and *Pressure Outlet* boundary conditions respectively. Additionally, the turbulence intensity is set to 0.01 and the turbulent viscosity ratio is set to 10 for both boundaries.

Symmetry boundary conditions are used on walls and roof, while the floor is set to a no-slip wall condition with a prescribed velocity of 120 kph to mimic moving ground. Tires and wheels are set to moving walls, rotating with a constant angular velocity around an axis placed through each wheel axis. The angular velocity is calculated according to

$$\frac{u}{r} = \frac{120/3.6}{0.318} = 104.8219\; rad/s, \tag{4.10}$$

where u is the linear velocity in [m/s] and r is the radius of the tire in [m]. The remaining stationary boundaries are set to no-slip wall boundary conditions. The computational domain is divided into several regions. The domain consist of the exterior air region, porous media regions for the heat exchangers and a separate region for the engine compartment. From overlapping boundaries, internal interfaces are created to couple the regions, according to Fig. [4.7].

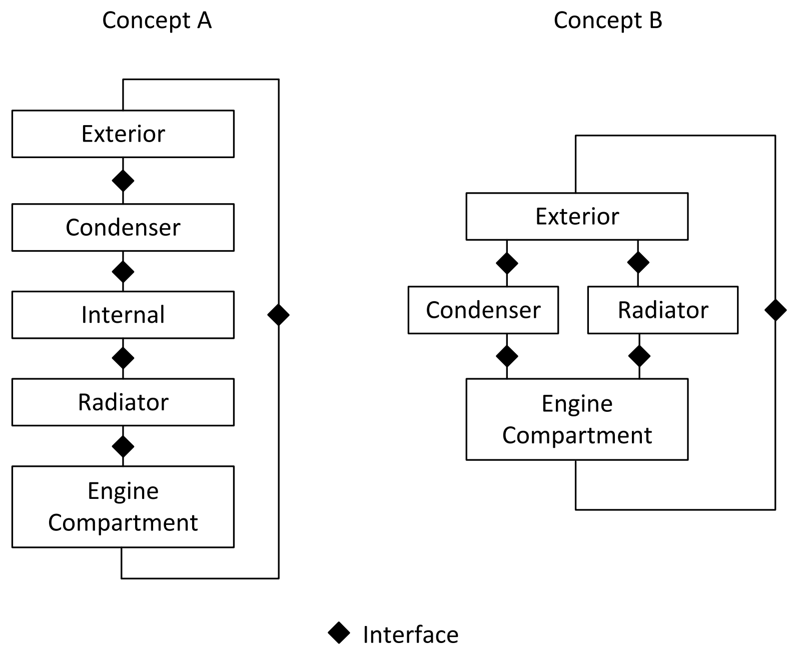

Figure 4.7: *Overview of the computational domain consisting of regions, which are connected by interfaces for both concepts.*

4.2.5 Solver settings

The iterative *Gauss-Seidel* method is used to solve the linear systems. In the pressure solver, the acceleration method *Conjugate Gradient* is used, which is recommended for incompressible flows using the segregated solver [31]. Under-relaxation factors of pressure, velocity, turbulence and the turbulent viscosity solver are set to 0.4, 0.5, 0.5, and 0.7 respectively.

All simulations are computed until the order of magnitude of the residuals is 10E-4 and the force coefficients and mass flow rate values are considered stable, which requires approximately 6000 iterations.

4.2.6 Post-processing

Final force coefficient and mass flow rate values are averaged over the last thousand iterations or more if its deemed necessary. *Scenes* and different types of *Displayers* are used for graphical visualization of geometry and flow field.

In order to make the post processing fast and efficient. A java macro is written to export the raw data and to create the scenes and export the desired pictures.

Additionally, non-dimensional quantities are used in the analysis of the result, which are defined below.

4.2.6.1 Force coefficients

In this work the forces acting on the vehicle are expressed as non-dimensional force coefficients. The longitudinal force is expressed as the drag coefficient C_d, which is defined as

$$C_d = \frac{F_d}{\frac{1}{2}\rho A V^2}, \tag{4.11}$$

where A is a characteristic area set to 2.16 m^2, ρ is the fluid density of air (1.18415 kg/m^3) and $V = 120$kph which is the free-stream velocity.

In this work the term *count* is often used referring to the drag which is defined as

$$0.001 C_d = 1\ count. \tag{4.12}$$

4.2.6.2 Cooling drag

The cooling drag is calculated by the absolute difference in vehicle drag coefficients between a specific cooling configuration and the configuration with closed grilles, i.e., no air-cooling of the under-hood.

4.2.6.3 Pressure coefficient

The dimensionless pressure coefficient describes the relative pressure in the flow field and is defined as

$$C_P = \frac{p - p_\infty}{\frac{1}{2}\rho_\infty V_\infty^2}, \tag{4.13}$$

where p is the pressure at the point of interest, p_∞ is the free-stream pressure and the denominator is the dynamic pressure in free-stream.

4.2.6.4 Normalized drag force of heat exchangers

In order to compare the aerodynamic drag contribution for heat exchangers with different frontal area, the drag forces generated have been normalized using the force from a reference case. The reference case is chosen to be A.3, see Section [5.1] for details. The normalized drag force of any heat exchanger is then given by

$$\hat{F}_{x,y} = \frac{F_{x,y}}{F_{x,A.3}} \tag{4.14}$$

where x can either be condenser or radiator and y is the configuration of interest.

5
Results

In this chapter the result for both concepts is presented. The attention is put on the mass flow rate across the heat exchangers, internal flow field and cooling drag. Results from the Concept A and Concept B will first be presented separately and afterwards compared with one another. The comparison will feature the configurations that obtained the lowest cooling drag, given a specific target for mass flow rate.

5.1 Concept A

In this section, result for all configurations of Concept A is presented. Each configuration have a unique combination of open/closed air inlets and outlets. For Concept A, there are two inlets available, upper and lower inlet. In Fig. [5.1], the different configurations with corresponding inlets and denotation can be seen.

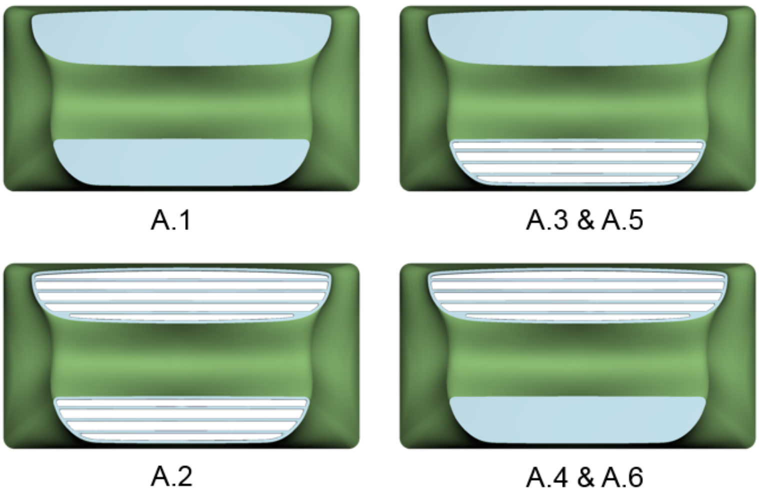

Figure 5.1: *Visualization of the different inlets for each configuration. The air guide (green) is kept identical for all configurations whereas the grille (grey) is either open or closed.*

Similarly, there are two types of available outlets. The first type of outlet is located at the drive shaft hole on each side of the engine compartment, this outlet is included in all configurations. The second outlet is placed on the floor of the engine compartment, this outlet is only added in configuration A.5 and A.6. The two different outlets can be seen in Fig. [5.2].

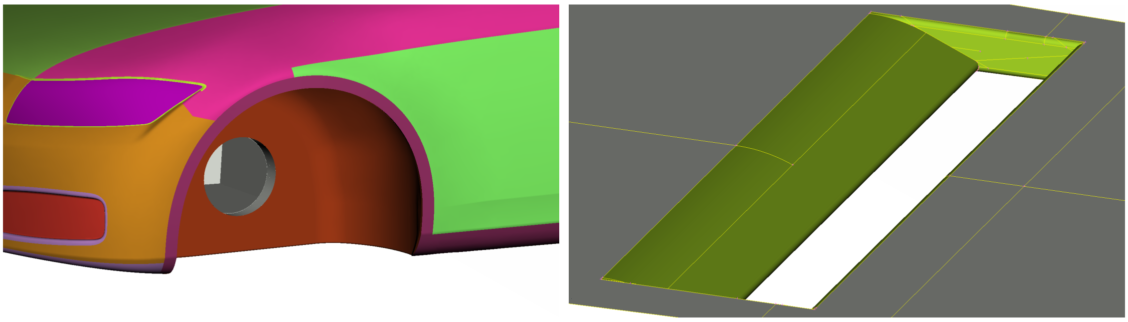

Figure 5.2: *Visualization of the standard outlet at the drive shaft holes (left) and the outlet through the floor of the engine compartment (right). The outlet at the floor is only included in configuration A.5 and A.6.*

5.1.1 Mass flow rate vs inlet area

The mass flow rate is measured as the mass of the air going through the cooling module. The inlet opening area is the projected frontal area of the inlet, i.e., the area projected on a surface with normal towards the flow direction. The mass flow rate and inlet areas for all configurations are measured in % with respect to the result of A.3 (lower grille open). The results of mass flow rate and corresponding inlet opening area can be seen in Fig. [5.3]. One can see that, closing any of the two

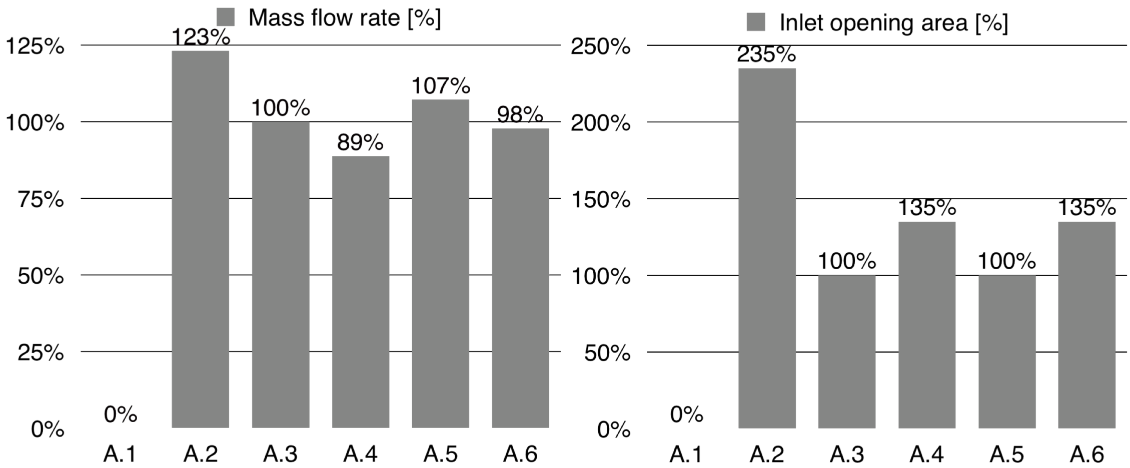

Figure 5.3: *Results of mass flow rate (left) and the measured inlet opening area (right) for all configurations of Concept A, measured in % with respect to that from A.3.*

grilles separately, will reduce the mass flow rate by 23 and 34 percentage points (pp) respectively (A.3 and A.4), compared with A.2. From the tables of Fig. [5.3], one can see that the lower grille configuration (A.3) provide higher mass flow rate with a smaller inlet area than that of the upper grille configuration (A.4). When both inlets are opened simultaneously (A.2), similar result is obtained. The lower inlet account for only 42% of the area, yet 67% of the mass flow rate, while the upper inlet account for 58% of the area and only 33% of the mass flow (Fig. [5.4]).

The additional outlet (left in Fig. [5.2]) featured in the last two configurations, seem to increase the total mass flow rate by 7 and 9 pp compared to A.3 and A.4 respectively. As a result, A.6 (upper grille + additional outlet) does almost (-2 pp) obtain the same mass flow as A.3 (lower grille).

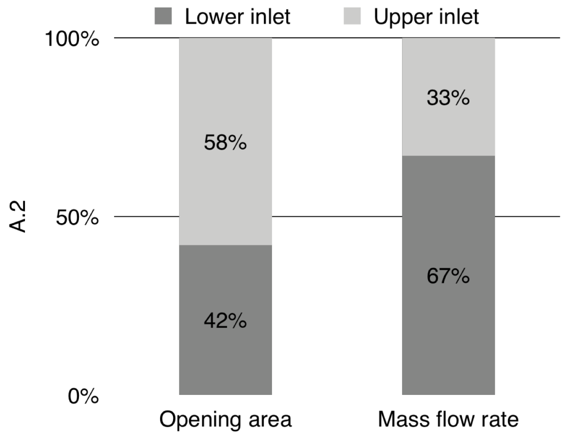

Figure 5.4: *The distribution of mass flow rate (right bar) and opening area (left bar) between the lower and upper inlets for configuration A.2.*

5.1.2 Flow field

The streamwise velocity component over the condenser interface for A.3 and A.4 can be seen in Fig. [5.5]. One can see that the areas with highest intensity is ob-

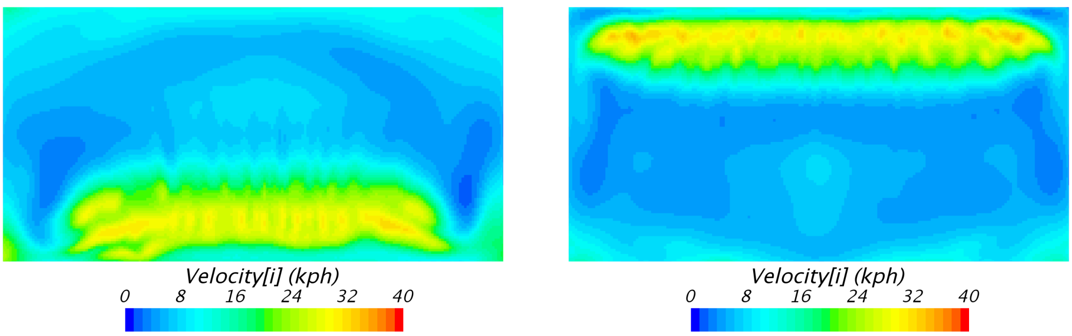

Figure 5.5: *The streamwise velocity component over the condenser interface for configurations A.3 (left) and A.4 (right), open lower and open upper inlet respectively.*

tained just behind the grilles, i.e., the yellow areas in Fig. [5.5]. Since the condenser interface is in such close proximity to the grilles, the air flow is not able to spread evenly over the whole interface. As a consequence, there exist regions of low mass flow rate across the heat exchangers (blue areas in Fig. [5.5]).

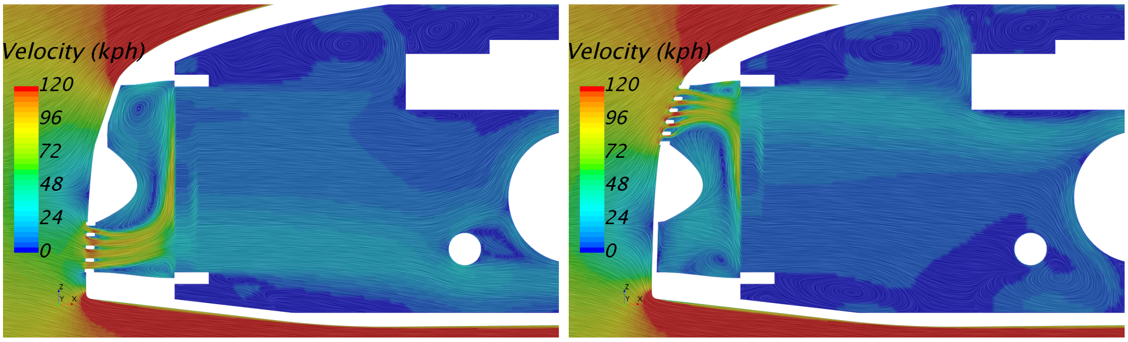

Figure 5.6: *Velocity magnitude plotted in a plane section located at y = 0m for A.3 (left) and A.4 (right).*

Interestingly, one can see a significant change in location of the stagnation point on the front-end of the vehicle as the inlet position is changed. The stagnation point can be interpreted as the small dark-blue region on the front of the car, close to the front impact structure and can be seen in Fig. [5.6]. It appears that the stagnation point is moving away from the position of the air inlet.

Additionally, the direction of the incoming cooling air is closer to horizontal for the lower inlet case (A.3) than for upper inlet case (A.4). As a result, the effective area for the upper inlet is significantly reduced and thus lower mass flow rate is obtained. This is due to the distance between the stagnation point and the lower inlet is much smaller.

When the air is approaching the interface of the heat exchanger, it also changes direction. Since the porous media makes it increasingly difficult for the air to pass through, much air is forced sideways (upwards and downwards), which can be seen in Fig. [5.6].

For configuration A.2, the mass flow rate is more evenly distributed over the condenser interface as air can enter from both the upper and lower inlet simultaneously, which can be seen in Fig. [5.7].

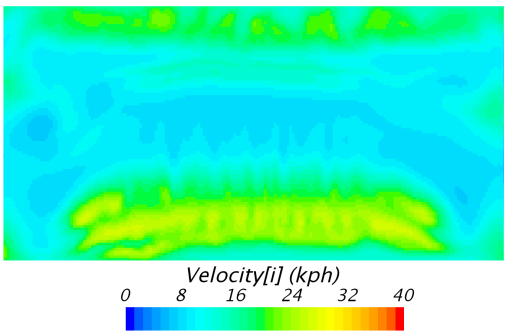

Figure 5.7: *Velocity profile at the condenser interface for configuration A.2.*

5.1.3 Cooling drag

The cooling drag is calculated by the difference in vehicle drag coefficients between the configuration of interest and A.1 (closed grilles). The cooling drag for each configuration can be seen in Fig. [5.8]. One can clearly see that configuration A.2,

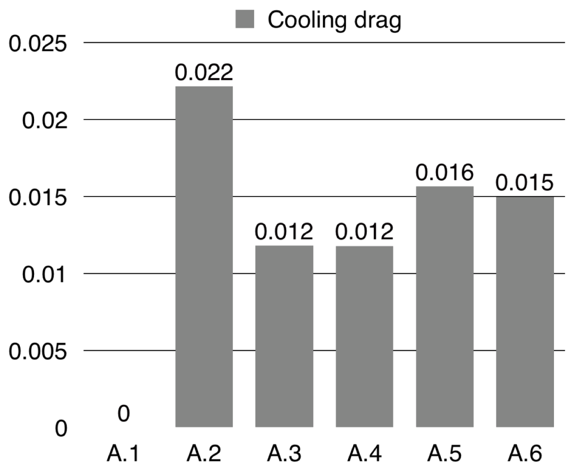

Figure 5.8: *Results of cooling drag for Concept A configurations.*

has the largest cooling drag penalty, which is expected due to high mass flow rate. Configurations A.3 and A.4 where the lower and upper grille is opened separately, the cooling drag is reduced down from 22 to 12 counts. Together with the previously presented result of the mass flow rate, one can quickly conclude that A.3 and A.4 provide the high mass flow rate to cooling drag ratio. For configurations A.5 and A.6 the cooling drag increased by 4 and 3 counts compared to A.3 and A.4, respectively.

5.2 Concept B

In this section, result for all configurations of Concept B is presented. Each configuration have a unique combination of open/closed air inlets and outlets. For Concept B, there are three inlets available, left, lower and right inlet. In Fig. [5.9], the inlets of each configuration and corresponding denotation can be seen. The configurations B.1 and B.2 consider all three inlets simultaneously. Configurations B.2 - B.8 are only considering the left and right inlets, while B.9 only consider the lower inlet.

The outlet located at the drive shaft hole is used in all configurations for Concept B. For configurations B.5 and B.8, the additional outlet have been added, which can be seen in Fig. [5.10].

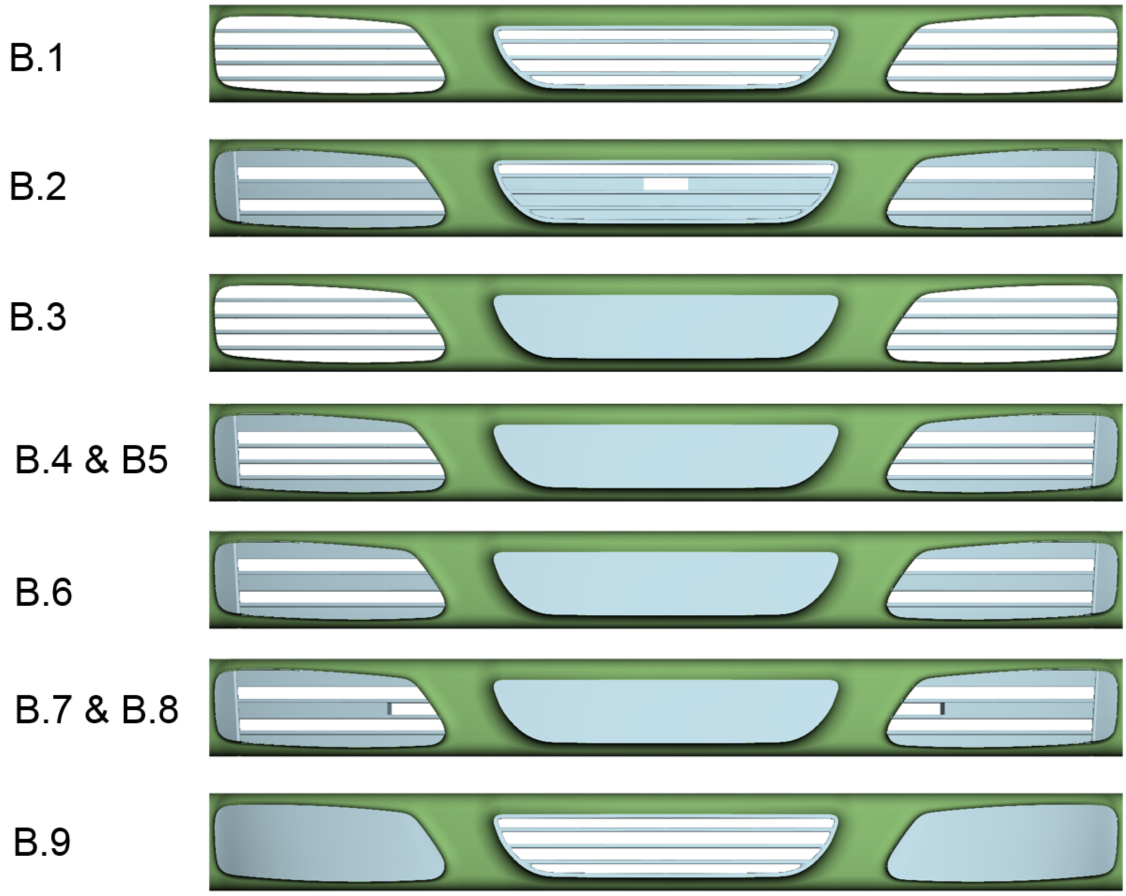

Figure 5.9: *Visualization of the different inlets for each configuration.*

Figure 5.10: *Visualization of the additional outlet, exiting air to the wheel houses. This outlet is added in configurations B.5 and B.8.*

5.2.1 Mass flow rate vs inlet area

The mass flow rate presented here is the mass flow going through the heat exchangers, i.e., the cooling module. Both the mass flow rate and the inlet areas presented are measured in % with respect to the result of configuration A.3, which is the reference case from Concept A. There are four configurations that are within a range of ±3% of the mass flow rate for the reference configuration A.3 from Concept A. These configurations are B.2, B.4, B.8 and B.9, see Fig. [5.11]. B.2 utilize a combi-

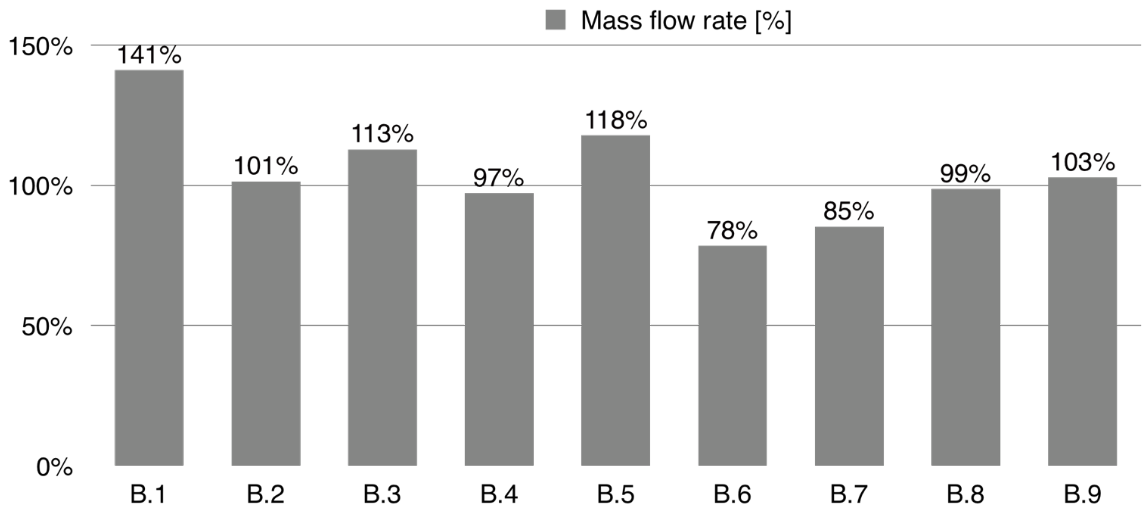

Figure 5.11: *Results of mass flow rate for Concept B configurations, measured in % with respect to that of A.3.*

nation of the left, lower and right inlet. In B.4, the the lower inlet is closed and in B.8, the additional outlet at the front arc of the wheel houses are included. B.9 is utilizing the lower inlet only. These four configurations are considered to be comparable to the reference case A.3. The remaining configurations providing mass flow rate which is too far above or below the target to be considered comparable with A.3.

The inlet opening areas for the four configurations are reasonably similar to the area of A.3 (lower grille open), except for B.8. The inlet area of B.8 is only 79% of A.3's inlet area, yet to obtain similar mass flow rate (99%). Which is due to the additional outlets, that enable less blockage and thus more air through the heat exchangers.

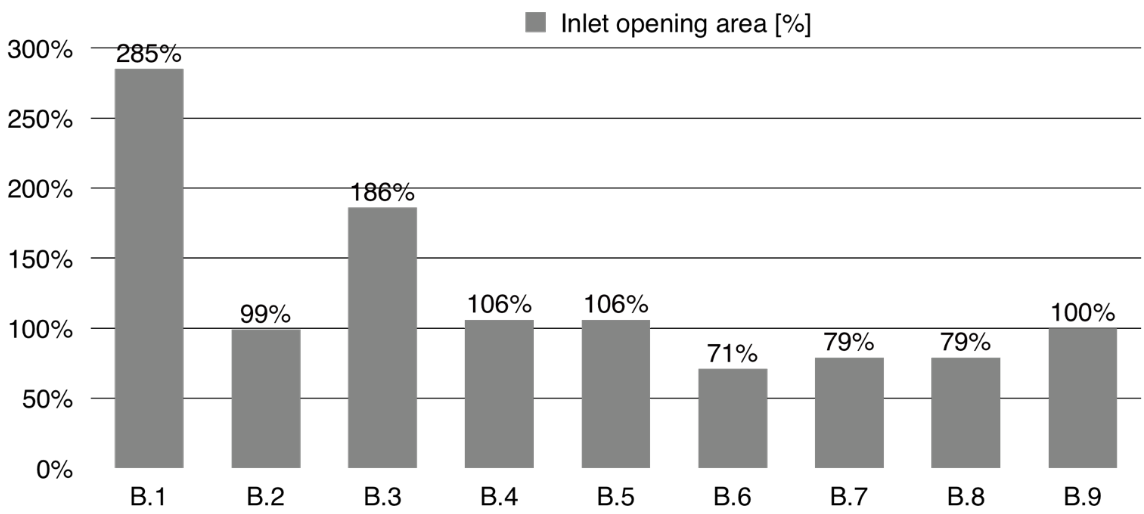

Figure 5.12: *Inlet opening area of Concept B configurations, measured in % with respect to A.3.*

5.2.2 Flow field

Similarly as obtained for Concept A, the regions of high mass flow rate across the heat exchangers are those in close proximity to the grilles, as we can see for B.4 in Fig. [5.13] and B.9 in Fig. [5.14]. Regions with low mass flow rate are located behind the closed inlets. By comparing these two configurations, the low intensity region of B.4 seems to be of smaller magnitude than corresponding low intensity region of B.9.

This can be explained by the direction of the incoming air towards the heat exchangers. When the lower grille is closed, approaching air is forced sideways through the side inlets, creating an angle with the center line. Thus, it becomes difficult for the air to turn back behind the closed lower inlet and then pass through the heat exchanger. In the opposite case when the lower inlet is open and side inlets closed. The air is from the beginning coming straight towards the heat exchangers and since the pressure on the heat exchangers is high, the air is naturally directed side ways behind the closed inlets. An additional reason could be distance form the inlet to the heat exchangers frontal surface, which is larger towards the middle of the vehicle.

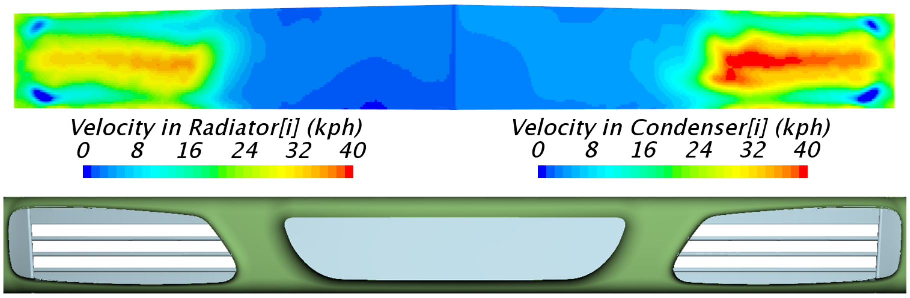

Figure 5.13: *Velocity profile at the radiator and condenser interfaces for configuration B.4.*

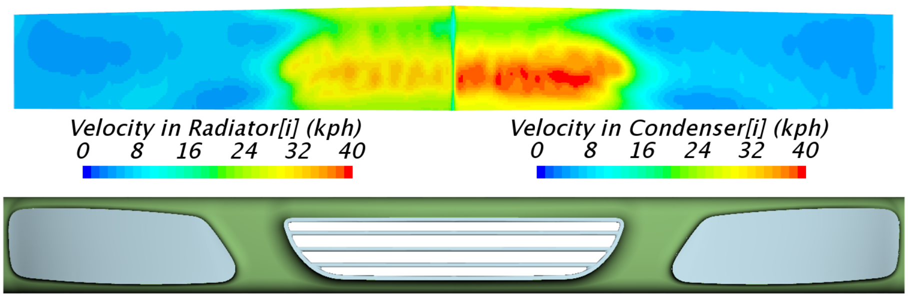

Figure 5.14: *Velocity profile at the radiator and condenser interfaces for configuration B.9.*

5.2.3 Cooling drag

The cooling drag is calculated in the same manner as for the previous concept. The cooling drag for configurations of Concept B can be seen in Fig. [5.15]. Configuration B.1, which provides most mass flow rate does also obtain the highest cooling drag (30 counts).

Out of the configurations of Concept B that is within a range of ±3% of the mass flow rate of the lower inlet configuration (A.3), B.8 obtained the lowest cooling drag (14 counts). The second lowest cooling drag configuration among this group (B.2, B.4, B.8 and B.9) are B.2 and B.4 with 19 counts each. Only two other configurations (B.6 and B.7) received lower cooling drag than B.8, which is probably due to the significantly lower mass flow rate (78% and 85%). Interestingly, B.5 obtained a lower cooling drag compared to B.4 by 2 counts, yet significantly higher mass flow rate (97% to 118%). The only difference between B.4 and B.5 is the additional outlet through the wheel house, which also appear to contribute successfully for B.8 as well. Unexpectedly the last configuration B.9, received a very high cooling drag (23 counts) compared to A.3 (12 counts), considering the inlets and outlets are identical.

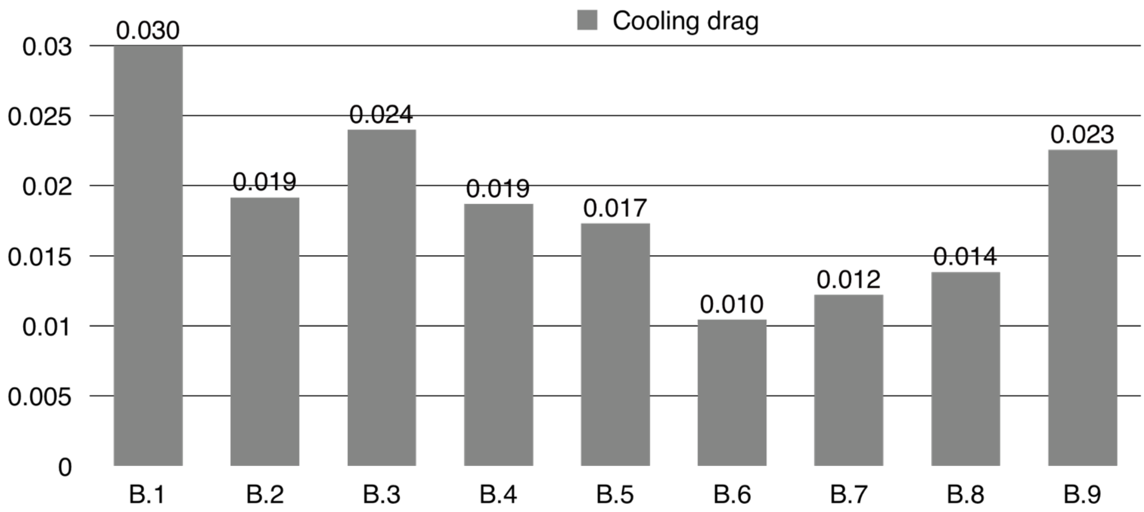

Figure 5.15: *Results of cooling drag for Concept B configurations.*

5.2.4 Comparison of B.7 and B.8

The geometrical difference between B.7 and B.8 is the outlet at the front arc of the wheel houses. As a result, the total mass flow rate increased. In addition, 77% of the exiting mass flow rate changed exit to the added outlets, completely changing the exit mass flow distribution. The mass flow distribution between the exits for B.7 and B.8 can be seen in Fig. [5.16]. The reason being that the outlets are positioned in close proximity behind the left and right inlets which create a natural way for the flow to exit. Another small observation about the flow is that the wake on the outside of the tire seems smaller. This can be seen by comparing the left and right pictures in Fig. [5.17], which visualizes the flow around the left inlet, tire, and outlets for B.7 and B.8. The flow direction downstream of the heat exchanger is significantly different between the two configurations which is confirmed by the table in Fig. [5.16]. However, the cooling drag difference is only 2 counts. In order to understand why, one can analyze the accumulation of aerodynamic drag. The accumulated drag

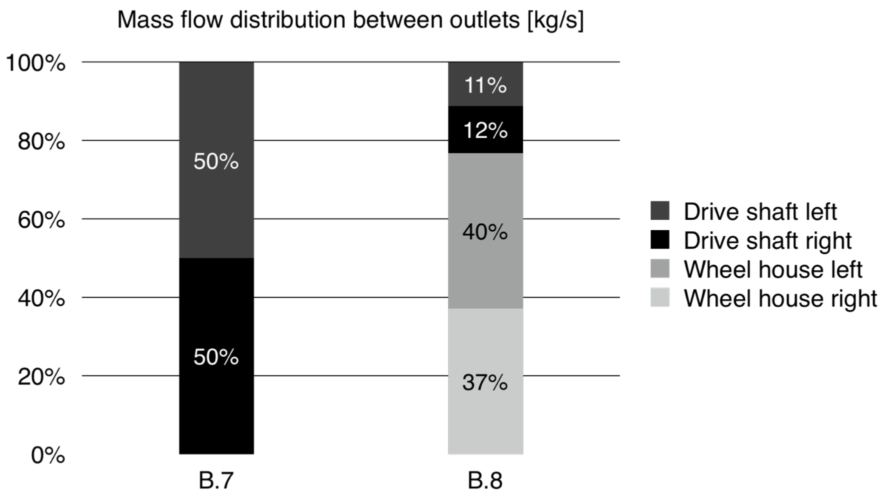

Figure 5.16: *Results of the distribution of mass flow rate between the outlets for configuration B.7 (left bar) and B.8 (right bar).*

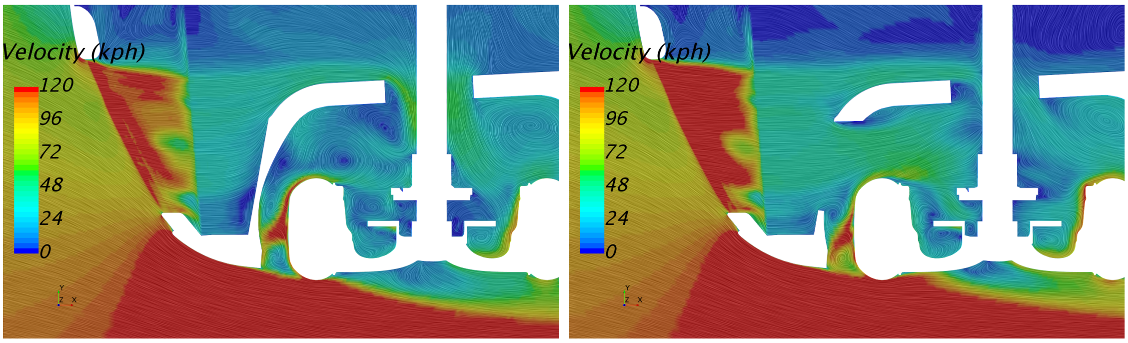

Figure 5.17: *Line integral convolutions in a plane section located at z = -0.01m visualizing the left inlet, front left tire and the air outlets. Left: B.7. Right: B.8.*

along the vehicle is compared between the configuration B.7 and B.8 is seen in Fig. [5.18]. One can see that the accumulated drag profile is almost identical downstream of the rear face of the engine compartment, yet a significant difference is observed upstream of that. Across the heat exchangers there is a large drag contribution observed for configuration B.8. Interestingly, a similar drag deduction can be seen at the rear face of the engine compartment. The additional outlets added for B.8 seems to generate a low pressure region inside the whole of the engine compartment, which initially contributing to drag as it is in contact with the front face of the engine compartment. The same low pressure region is also in contact with the rear face of the engine compartment which can explain the local drag deduction. The low pressure region inside the engine compartment is visualized in light blue to the right in Fig. [5.19].

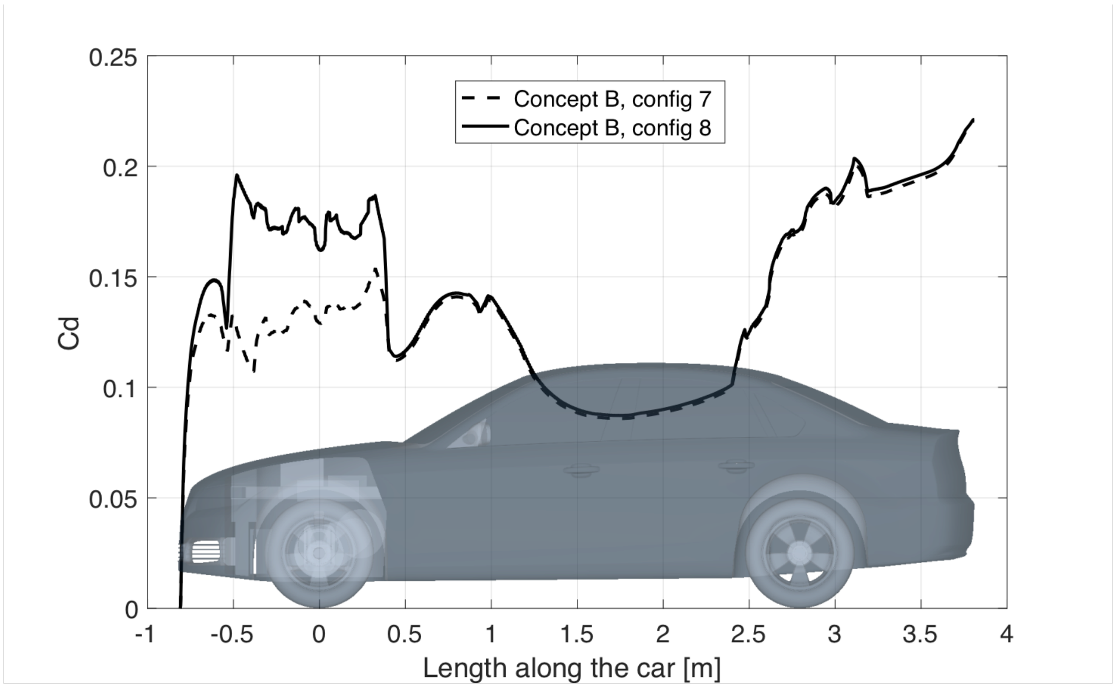

Figure 5.18: *Accumulated drag coefficient along the vehicle for B.7 and B.8.*

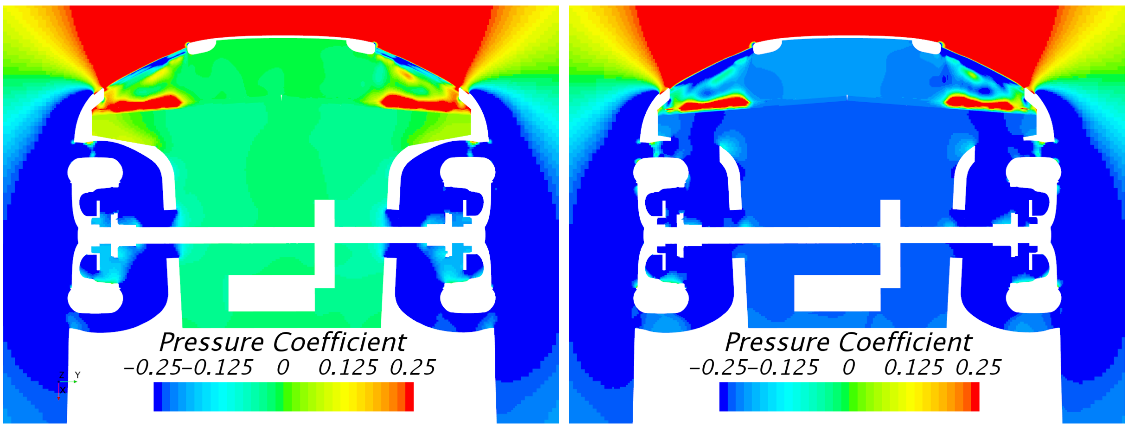

Figure 5.19: *Pressure coefficient in a plane section located at z = -0.01m showing the engine compartment, front tires and front-end of the car for B.7 (left) and B.8 (right).*

5.3 Concept comparison

In this section a comparison between Concept A and Concept B is presented. The comparison is between A.3 (reference case) and B.8 (side inlets + additional outlet) which produced the lowest cooling drag among the configurations of Concept B which reached the target of mass flow rate. Cooling drag contribution, forces over heat exchangers, inlet opening areas and mass flow rate distribution will be compared.

As the total mass flow rate is considered equal (difference of 1%) between the two configurations, it will be neglected in the comparison.

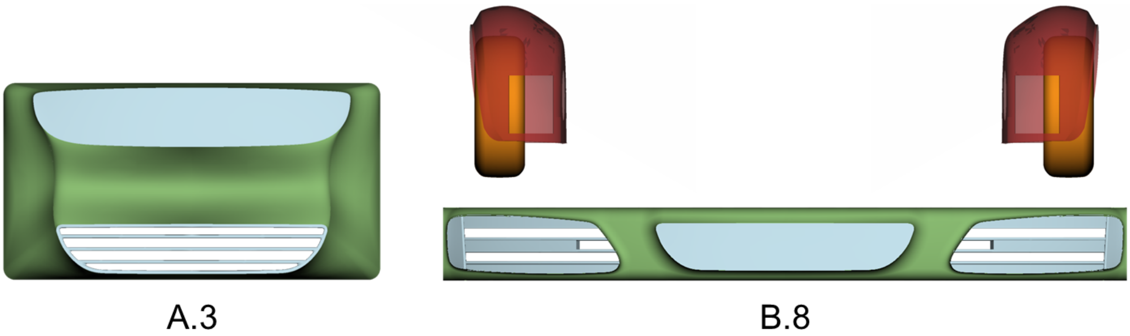

Figure 5.20: *Visualization of the difference between inlets and the outlets for configuration A.3 and B.8.*

5.3.1 Cooling drag and drag contribution from heat exchangers

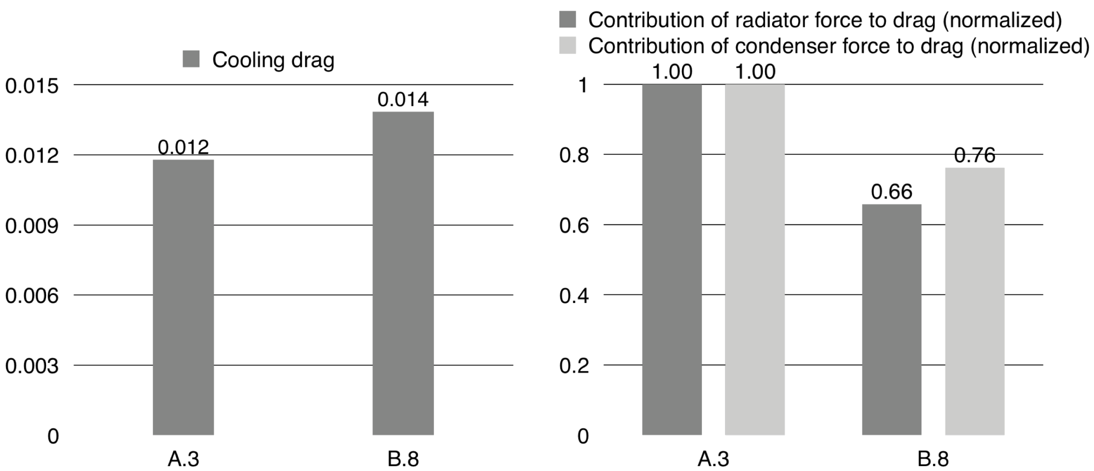

Figure 5.21: *Comparison of cooling drag (left) and contribution of heat exchanger force to drag (right) for A.3 and B.8.*

In Fig. [5.21] the cooling drag and the contribution of heat exchanger force to drag are compared. One can see that the cooling drag for A.3 is only 2 counts lower than that of B.8. However, the drag induced from the heat exchangers of configuration B.8 is significantly lower than that of A.3. Similar results are observed in general for both concepts. As the porous regions are identically set up regarding thickness and pressure drop, it is probably the smaller frontal area of the heat exchangers in B.8 which results in lower drag contribution.

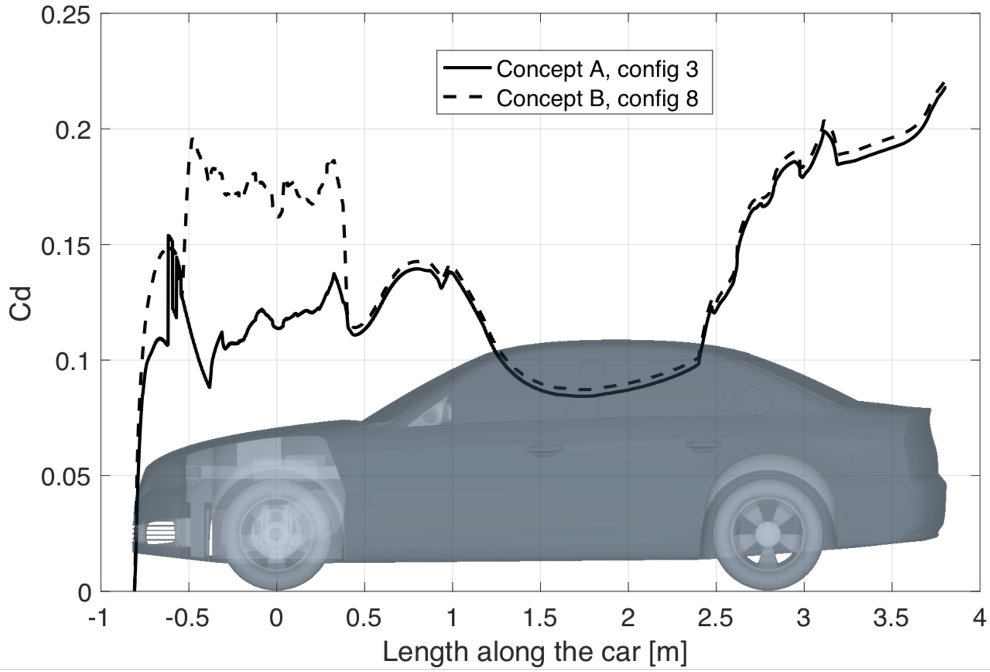

Figure 5.22: *Accumulated drag coefficient along the vehicle for A.3 and B.8.*

5.3.2 Global drag contribution

In order to analyze the difference in contribution of drag between the concepts, the accumulated drag coefficient along the vehicle is plotted for A.3 and B.8 in Fig. [5.22]. One can clearly see that there is a significant difference in drag contribution at the front of the vehicle. Firstly, one can see that the front bumper of B.8 has larger contribution than that of A.3. The drag contribution from the heat exchangers in series is then clearly seen for Concept A. However, for Concept B, the corresponding drag contribution is not entirely from the heat exchangers, but also from the low pressure area inside the engine compartment acting on the front face of engine compartment which was observed earlier in Fig. [5.19]. The same low pressure region act on the rear face of the engine compartment which causes the local drag deduction. Similar drag deduction is seen for concept A but at a smaller magnitude, which can be explained by the relatively higher pressure inside the engine compartment seen to the left in Fig. [5.23]. Downstream of the engine compartment the drag contribution is fairly similar for both configurations which is expected due to identical geometries.

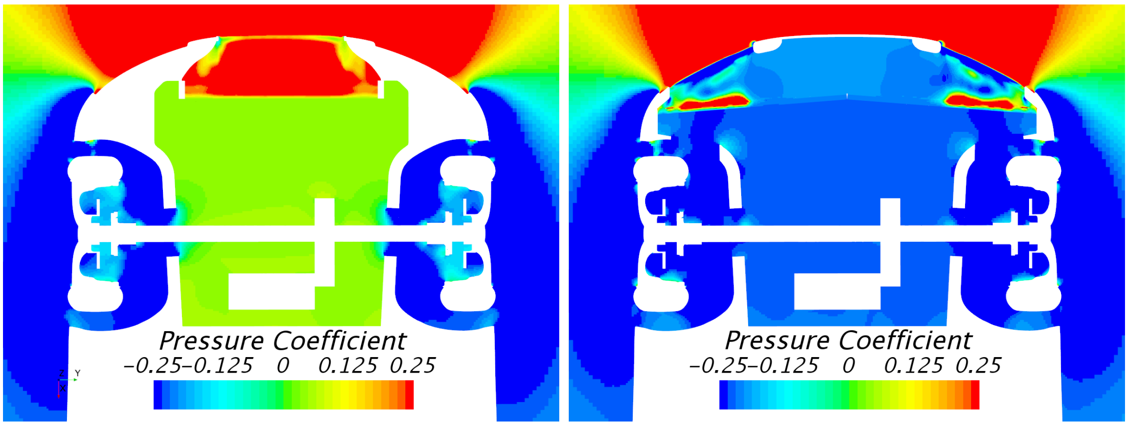

Figure 5.23: *Pressure coefficient in a plane section located at z = -0.01m showing the engine compartment, front tires and front-end of the car for A.3 (left) and B.8 (right).*

6
Discussion

In this chapter, different aspects of the concepts, geometry, computational method and future work are discussed.

6.1 Concepts

The results presented in the previous chapter show potential for various cooling flow solutions and positioning of heat exchangers. Especially towards low positioned inlets but also inlets positioned on the outer part of the front bumper in combination with outlets located at the front arc of the wheel houses. The difference in cooling drag between Concept A and Concept B was 2 counts, which is considered to be well within the uncertainty of the computational method. This increases the difficulties to suggest one cooling flow solution over the other. However, both of the solutions have advantages and disadvantages on the thermal management as a whole. Positioning the heat exchangers in parallel, more than a single fan is most likely required to fulfill thermal requirements at stand still condition. On the other hand, parallel heat exchangers will provide the highest temperature difference between the coolant of the heat exchangers and ambient air, maximizing the heat transfer. This can be particularly important in warm conditions when the temperature difference is very small. Additionally, distributing air-flow on demand becomes increasingly easier using e.g., active grille shutters for parallel positioned heat exchangers, whereas in-series, both heat exchangers would inevitably be affected equally.

6.2 Geometry

The exterior geometry is taken from the realistic generic notchback DrivAer Model which is considered a good approximation of a real notchback vehicle. The engine compartment box is originally designed for an ICEV, which together with the simplified electric propulsion system, leaving a large void area inside the engine compartment. This void is believed to be larger than for a real BEV. For this reason, there will be less blockage from the propulsion system and the engine compartment which will effect the flow field, thus also the results. Whether the geometry of the engine compartment is more beneficial for Concept A or Concept B, is difficult to conclude. It is also difficult to determine the effect on the results from the difference between the modeled and the real geometry.

Fan, fan shroud, air guide and heat exchangers are factors with great influence on thermal aspects (Section 2.3). The fan and fan shroud was discarded for both concepts in order to eliminate factors of uncertainty of the influence on each concept separately. The influence of the fan shroud and fan geometry would be difficult to measure as the heat exchanger dimensions was changed from Concept A to Concept B. As the dimensions changed, the air guide was changed accordingly. Geometry from the air guide of Concept A was used to create the air guide for Concept B. By analyzing the flow field inside the air guide for both concepts, it is however clear that neither of the air guides are well optimized as air immediately separates inside the guide.

6.3 Computational method

Previous studies have shown that the RANS method have consistently underpredicted drag coefficients of external aerodynamics of passenger cars [27]. For this reason, one can not be certain that prediction of drag for each configuration and concept is performed with the similar magnitude of error. In addition, no mesh independence study have been performed during this work. However the mesh is believed to be of good quality according to the recommendations of the software's developer.

6.4 Future Work

Future work can for example be to run the simulations featuring lesser geometrical difference between the modeled and real geometry if possible. At the moment the engine bay is too empty and not realistic, a more accurate representation of an engine bay is desired. Secondly, careful positioning of heat exchangers, inlets and outlets is to be preferred while simultaneously considering the vehicle concept and other subsystems. One can also choose to add the energy equation in the CFD method in order to evaluate the thermal aspects of the heat exchangers.

Additionally, a third concept was planned including air inlets in close proximity to the rear wheels and heat exchangers positioned behind the cabin towards the rear bumper.

7
Conclusion

In this project, two thermal management concepts have been evaluated. The study evaluates two conceptually different approaches of positioning heat exchangers in an electric vehicle, in series and in parallel. For each concept, different air inlet and outlet positions have been investigated. Vertically positioned inlets have been considered in the first concept (in series) and horizontally positioned, in the second concept (in parallel). In total, 15 design configurations have been investigated through CFD in order to determine the concept and corresponding design configuration providing the lowest cooling drag for a given mass flow rate.

For the concept with heat exchangers in series, results showed that the configuration with low positioned cooling inlet was the most drag efficient configuration. Additionally, the lower inlet provided higher mass flow through a smaller inlet opening area compared to the upper inlet, which coincide with previous studies [23].

For the second concept with heat exchangers in parallel, the design configurations with side positioned inlets, including air outlets located at the front arc of the wheel houses was shown to be the most successful with difference in cooling drag of 2 counts.

Finally, even though the results show similarly low drag coefficients, considering the discussion about the concepts in Section [6.1], the concept of parallel heat exchangers is considered to be at an advantage.

Bibliography

[1] Grunditz, E., and Thiringer, T., (2016): *Performance Analysis of Current BEVs Based on a Comprehensive Review of Specifications*. IEEE Transactions on Transportation Electrification, Vol. 2, No. 3, 2016, pp. 270 - 289.

[2] IEA, EVI., (2016): *Global EV Outlook 2016*. URL: `https://www.iea.org/publications/freepublications/publication/Global_EV_Outlook_2016.pdf`. [Accessed 2017-04-28].

[3] Nykvist, B., and Nilsson, M., (2015): *Rapidly falling costs of battery packs for electric vehicles*. Nature Climate Change, Vol. 5, 2015, pp. 329–332.

[4] Katerina E. Aifantis, Stephen A. Hackney, R. Vasant Kumar. *High Energy Density Lithium Batteries: Materials, Engineering, Applications*. John Wiley & Sons, 2010.

[5] Wiebelt, A., and Neumeister, D., (2013): *Progress in vehicle Aerodynamics and Thermal Management*. Proceedings of the 9th FKFS Conference Stuttgart, 2013, pp. 24 - 33.

[6] Thomas, J., (2014): *Drive Cycle Powertrain Efficiencies and Trends Derived from EPA Vehicle Dynamometer Results*. SAE Int. J. Passeng. Cars - Mech. Syst, Vol. 7, No. 4, 2014, pp. 1374-1384.

[7] Chan, C, C., (2002). *The State of the Art of Electric and Hybrid Vehicles*. Proceedings of the IEEE, Vol. 90, No. 2, 2002, pp. 247 - 275.

[8] Kia.com URL: *http://www.kia.com/us/en/vehicle/soul-ev/2016/features*. [Accessed 2017-03-27].

[9] Shimizu, H., Okubo, T., Hirano, I., Ishikawa, S. and Abe, M,. *Development of an Integrated Electrified Powertrain for a Newly Developed Electric Vehicle*. SAE Technical Paper 2013-01-1759.

[10] Hyundai Sweden. URL: `http://www.hyundai.se/bilar/ioniq-elbil`. [Accessed 2017-03-27].

[11] Ruoho, S., Kolehmainen, J., Ikaheimo, J. and Arkkio, A,. *Interdependence of Demagnetization, Loading, and Temperature Rise in a Permanent-Magnet Synchronous Motor*. IEEE Transactions on Magnetics, Vol. 46, No. 3, 2010, pp. 949 - 953.

[12] Patent number: US20100025006 A1 (2009). *Electric vehicle thermal management system*. Tesla Motors, Inc.

[13] Nissan Motor Corporation. URL: `http://www.nissan-global.com/EN/TECHNOLOGY/OVERVIEW/heat_pump_cabin_heater.html`. [Accessed 2017-03-23].

[14] Renault Sweden. URL: `https://www.renault.se/bilar/personbilar/nya-zoe/räckvidd.html`. [Accessed 2017-03-23].

[15] BMW Media Information. *The BMW i3*. July, 2013. URL: `https://www.press.bmwgroup.com/global/article/detail/T0143924EN/the-bmw-i3`. [Accessed 2017-03-23].

[16] Juan, T., (2008). *Investigation and Assessment of Factors Affecting the Underhood Cooling Air Flow Using CFD*. SAE Technical Paper 2008-01-2658.

[17] Simonin, M., Marsais, C., Palier, P., and Borowski, W., (1988). *A New Approach to Sizing and Packaging of the Heat Exchangers for the Passenger Car*. SAE Technical Paper 880049.

[18] Christoffersen, L., Löfdahl, L., and Jönson, A., (2010). *Interference between Engine Bay Flow and External Aerodynamics of Road Vehicles*. SAE Technical Paper 2010-01-0288.

[19] Tortosa, N., and Karbon, K., (2011): *Aerodynamic Development of the 2011 Chevrolet Volt*. SAE Int. J. Passeng. Cars – Mech. Syst, Vol. 126, No. 2, 2011, pp. 166-171.

[20] Zhang, C., Uddin, M., Song, X., Fu, C., et al., (2016): *Simultaneous Improvement of Vehicle Under-Hood Airflow and Cooling Drag Using 3D CFD Simulation*. SAE Technical Paper 2016-01-0200.

[21] Saab, S., Hetet, J., Maiboom, A., and Charbonnelle, F., (2013). *Impact of the Underhood Opening Area on the Drag Coefficient and the Thermal Performance of a Vehicle*. SAE Technical Paper 2013-01-0869.

[22] Palin, R., Johnston, V., Johnson, S., D'Hooge, A. et al., (2012): *The Aerodynamic Development of the Tesla Model S - Part 1: Overview*. SAE Technical Paper 2012-01-0177.

[23] Wittmeier, F. and Kuthada, T., (2015): *Open Grille DrivAer Model - First Results*. SAE Int. J. Passeng. Cars - Mech. Syst, Vol. 8, No. 1, 2015, pp. 252-260.

[24] Heft, A., Indinger, T., and Adams, N., (2012): *Introduction of a New Realistic Generic Car Model for Aerodynamic Investigations*. SAE Technical Paper 2012-01-0168.

[25] Technical University of Munich. Institute of Aerodynamics and Fluid Mechanics. URL: `https://www.aer.mw.tum.de/en/research-groups/automotive/drivaer/`. [Accessed 2017-03-23].

[26] Shinde, G., Joshi, A., and Nikam. K., (2013): *Numerical Investigations of the DrivAer Car Model using Opensource CFD Solver OpenFOAM*. Conference: OSCIC 13, At Hamburg, Germany, 2013.

[27] Ashton, N., West, A., Lardeau, S., and Revell, A., (2016): *Assessment of RANS and DES methods for realistic automotive models*. Fluid & Computers. 2016.

[28] Shih, T. H., Liou, W. W., Shabbir, A., Yang, Z., and Zhu, J. (1995). *A new k-ε eddy viscosity model for high reynolds number turbulent flows*. Computers & Fluids, Vol. 24, No. 3, pp. 227-238.

[29] CD-adapco. STAR-CCM+ User Guide/Modeling Physics/Modeling Turbulence/Wall Treatment (2017). URL: `https://stevedocs.cd-adapco.com`. [Accessed 2017-05-03].

[30] CD-adapco. STAR-CCM+ User Guide/Theory Guide/Porous Media (2017). URL: `https://stevedocs.cd-adapco.com`. [Accessed 2017-03-23].

[31] CD-adapco. STAR-CCM+ User Guide/Theory Guide/Numerical Flow Solution/Finite Volume Discretization/Algebraic Multigrid (2017). URL: `https://stevedocs.cd-adapco.com`. [Accessed 2017-05-15].

A
Appendix

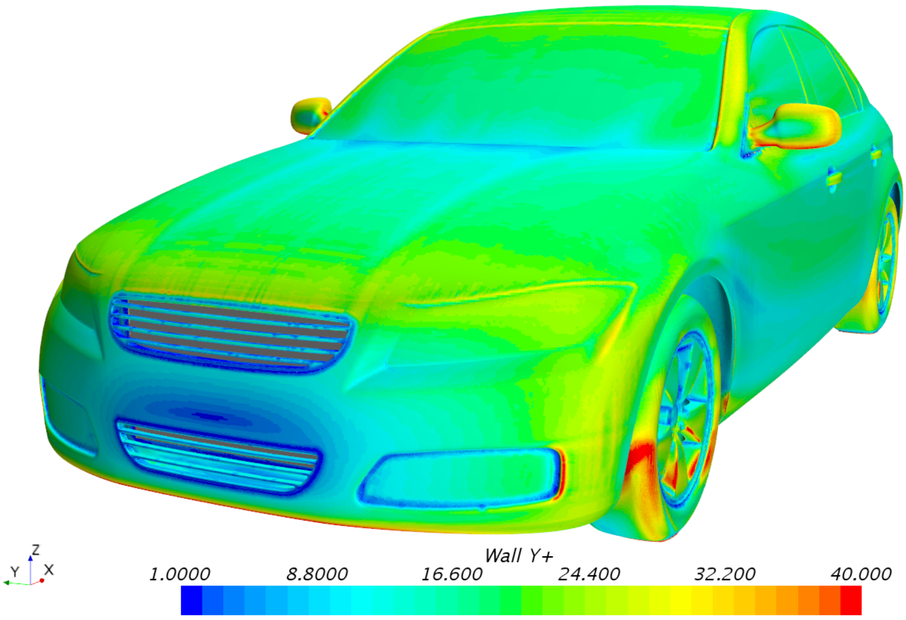

Figure A.1: *Wall y^+ values cut in range of $[1, 40]$ for the exterior of the car.*